



Experiments on the unsteady massive separation over an aerofoil

S. Mohamed Aniffa  and Alakesh Ch. Mandal **Department of Aerospace Engineering, Indian Institute of Technology, Kanpur 208016, India*

(Received 5 March 2023; accepted 7 November 2023; published 7 December 2023)

We have experimentally investigated an unsteady separating flow over a NACA-0012 aerofoil. Both the surface pressure measurements and the whole flow field measurements using the time-resolved particle image velocimetry (TR-PIV) technique were carried out at different angles of attack for a chord-based Reynolds number, $Re_c = 5 \times 10^4$. The instantaneous flow fields were measured at the stall angle of attack ($\alpha = 10^\circ$) and at different post-stall angles of attack ($\alpha = 11^\circ, 12^\circ, 13^\circ$) using the TR-PIV system. Although the mean flow data, as expected, show that the flow is fully/massively separated for $\alpha > 10^\circ$ over the suction surface of the aerofoil, the time sequence of the instantaneous flow fields reveals that the massive separation is intermittent in nature. A small separated region grows with time, eventually leading to the massive flow separation and then the massively separated region decays with time leading to a small separated region. In this process, the vortex shedding from the separated shear layer is also observed. We find that an interplay exists between the temporal growth of the separated shear layer and the vortex shedding during the intermittent massive separation. The mechanism for the intermittent massive flow separation has been explained using the time sequence of the instantaneous flow fields. This has further been supported using the proper orthogonal decomposition analysis. Furthermore, the spatiotemporal stability analysis of the local velocity profile shows that when the small separated region goes to a fully separated state, the velocity profiles become absolutely unstable from a convectively unstable state, and vice versa. In addition, these results are found to be consistent with the absolute instability criteria proposed in Alam and Sandham [*J. Fluid Mech.* **410**, 1 (2000)] and Avanci *et al.* [*Phys. Fluids* **31**, 014103 (2019)].

DOI: [10.1103/PhysRevFluids.8.123901](https://doi.org/10.1103/PhysRevFluids.8.123901)

I. INTRODUCTION

Flow separations are often encountered in various engineering devices; for example, flow separation may occur inside the inlet duct of a gas turbine engine, over the deck of a ship, over the wing of an aircraft, the cross-section of which has an airfoil shape. Applications of micro air vehicle (MAV), unmanned air vehicles (UAV), and wind turbines, which usually operate at a low Reynolds number, i.e., $Re_c < 10^6$ [1,2], are also increasing progressively. Design of these engineering devices involves various types of airfoils. The flow over these airfoils remains stable and attached at a lower angle of attack. As the angle of attack increases, the attached shear layers may separate due to the adverse pressure gradient. The separated shear layer further reattaches downstream and forms an enclosed region, which is called a separation bubble. The structure of the separation bubble is proposed by Horton [3] (in the time-averaged sense), which comprises the fore and rear parts. In the fore part of the bubble, the flow is nearly steady, and the pressure is nearly constant. However, the pressure recovery occurs in the rear part of the bubble due to the transition to turbulence.

*Corresponding author: alakeshm@iitk.ac.in

A separation bubble is often classified as a short or a long bubble [4,5]. In a short bubble, a small plateau is observed in the pressure distribution over the upper surface of an airfoil. Moreover, the pressure distribution for a short bubble nearly resembles the pressure distribution corresponding to the potential flow. In contrast, the constant plateau of the pressure distribution is extended in the entire upper surface of an airfoil for a long bubble, and this distribution is seen to deviate considerably from the pressure distribution corresponding to the potential flow [5].

The process of a sudden change from a short bubble to a long bubble formation is called bubble bursting, which occurs either due to an increase in the angle of attack or due to a reduction in the flow velocity to a certain value [4,6]. Several semi-empirical relations are proposed to predict the bubble bursting. Owen and Klanfer [4] proposed a criterion using the Reynolds number ($Re_{\delta^*,s}$) based on the displacement thickness (δ^*) and the free-stream velocity at the point of separation (U_s). However, Gaster [6] proposed a criterion using two parameters, i.e., the pressure gradient parameter and the Reynolds number ($Re_{\theta,s}$) based on the momentum thickness at the separation location (θ_s) and U_s . Diwan *et al.* [7] revisited the bursting criteria of the previous works and refined the criterion of Gaster [6] using the maximum height of the bubble. These bubble bursting criteria are proposed based on the time-averaged pressure and velocity data. However, the details of the flow field under this situation are missing in the literature.

Several authors report the presence of low- and high-frequency unsteadiness in the separated flows [e.g., Refs. [8–11]]. It is adequately understood that the vortex shedding from the separated shear layer due to the Kelvin-Helmholtz instability leads to the high-frequency unsteadiness [e.g., Refs. [12–14]]. In contrast, the cause of the low-frequency unsteadiness is not well understood, as compared to the high-frequency unsteadiness. In various studies, it was observed that the vertical oscillation of the separated shear layer causes the low-frequency oscillation, which is called flapping [15–18]. Moreover, it has been reported that bubble bursting is one of the reasons for the low-frequency unsteadiness [11]. In this process, a quasi-periodic switchover from a short to a long bubble leads to low-frequency unsteadiness. In particular, the growth and decay of a separation bubble cause low-frequency oscillation.

A near stall study of an airfoil shows that the value of the lift coefficient, C_L , oscillates due to the bubble growth and decay [19,20]. The oscillation amplitude of C_L depends on the angle of attack and Re_c . Almutairi *et al.* [21] reported that the amplitude of the low-frequency oscillation increases with the angle of attack and Re_c . However, this amplitude does not monotonically increase with the angle of attack. This attains the maximum value only in a certain range of angle of attack [2]. The reason was summarized as follows: Short bubble forms near the leading edge at an angle of attack less than the stall angle. As the angle of attack increases beyond the stall angle, the trailing edge bubble forms near the trailing edge of an aerofoil. Further increasing the angle of attack, this leading and trailing edge bubble is merged intermittently. This intermittent merging causes a prominent low-frequency oscillation over an aerofoil. If the angle of attack increases beyond this state, both the bubbles merge together and form an open bubble/completely separated state. Hence, the amplitude of the low-frequency oscillation is decreased. The above summary is based on the phase-averaged streamlines. However, the evolution of growth/decay of the separation bubble and its vortex shedding characteristics during the low-frequency oscillation has not been reported by Eljack *et al.* [2].

The growth and decay of a separation bubble are linked to the absolute instability of the separated shear layer. To find the presence/absence of absolute instability, the maximum reverse flow velocity (MRV) is used as a main parameter. Moreover, different threshold values are proposed for the occurrence of absolute instability based on MRV of one-dimensional (1D) and two-dimensional (2D) velocity profiles. Considering the family of modified Falkner-Skan separating velocity profiles, Hammond and Redekopp [22] found $MRV \sim 30\%$ for the onset of the absolute instability, whereas considering the local mean velocity profiles at a particular streamwise location from their two dimensional direct numerical simulation, Alam and Sandham [23] reported $MRV > 15\text{--}20\%$ for the onset of absolute instability. Recently, Rodriguez *et al.* [24] studied the laminar separation bubbles using linear stability analysis and direct numerical simulation. Their stability analysis of the 2D

velocity profiles in the cross-stream planes (i.e., velocity is dependent on two spatial coordinates) shows $MRV > 7\%$ for the onset of absolute instability. In many of the airfoil studies, Alam and Sandham [23] criterion was used to investigate the absolute instability and found to hold well during the formation of a long bubble. This leads to the conclusion that absolute instability is the main reason for the bubble bursting [2,11,19]. However, the large eddy simulation of Alferez *et al.* [25] shows that the absolute instability criterion holds good even for a short bubble. This observation led them to conclude that the height of the separated shear layer from the wall is also important for the bursting process, consistent with the study of Marxen and Henningson [26]. Movement of the transition location during the bursting process is also found to be different. The transition location is seen to move upstream and close to the wall during the decay of the bubble, whereas it moves downstream and away from the wall during the growth of the bubble [19]. This clearly indicates that the height of the shear layer is an important parameter in the transition process. Our recent study on the separated shear layer over a flat plate also shows that the vertical oscillation of the separated shear layer leads the vortex shedding process to be intermittent [27]. However, the convective/absolute instability characteristics of a separated shear layer during its vertical oscillation were not investigated, which certainly invites further studies.

The amplitude of the input disturbance and the forcing frequency can also affect the state of a separation bubble [26,28]. An increase in the disturbance amplitude can reduce the bubble dimension, whereas it increases with decreasing the amplitude of the input disturbance, leading to a long bubble state, which resembles the bubble bursting process [26]. This clearly shows that a minimum amount of disturbance amplitude is required to maintain the bubble in a short bubble state. In the absence of any forcing, the two-dimensional (2D) rollers are found to be absent, whereas these are found to be present with the increasing forcing frequency or amplitude of the input disturbance, leading to the conclusion that an increase in the forcing frequency or in the amplitude of the input disturbance can suppress the absolute instability and promotes coherency of the 2D roller formation [28]. Thereby, the bubble bursting process or the formation of a long bubble can also be linked with the transitional structures at the maximum height of the bubble. While a regular periodic vortex structure is seen to be present for a short bubble, it is found to be absent in the case of a long bubble [6,26,29].

As reviewed above, the growth and decay of a separation bubble over an airfoil can result in the intermittent formation of an open or a closed separation bubble, respectively. In this process, the temporal growth of a separation bubble and the vortex shedding are the two important phenomena. But, how these two phenomena are interlinked, and the associated physical mechanism of this intermittent massive separation is not available in the literature. Therefore, we aim to investigate the following: How do the temporal growth and the vortex shedding of the separated shear layer contribute to this intermittent massive separation? How do the instantaneous flow field and its stability characteristics change in this process?

II. EXPERIMENTAL SETUP

All the experiments reported here are performed in a closed circuit wind-tunnel, details of which are available in Refs. [30,31]. Briefly, the length, height and width of the test section are 1.520 m, 1.220 m, and 0.305 m, respectively. The tunnel is powered by a 15 HP DC motor, and the maximum velocity attained in the test section is 52 m/s. Since we aim to investigate the unsteady characteristics of a separation bubble, an airfoil, NACA-0012, was chosen following other studies [2,11,21,32–34]. The chord length (c) of the aerofoil was 160 mm, which spanned the entire width of the test section, and it was placed at the center of the wind-tunnel test section. The aerofoil angle of attack (α) was adjusted by rotating a shaft which passed through its quarter chord point. The shaft was rotated with the help of a servo motor with an uncertainty of $\pm 0.4^\circ$. The pressure taps at the midspan of the aerofoil were connected to the ESP-32HD piezo-resistive pressure scanners, which have an accuracy of $\pm 0.07\%$. The differential pressure, Δp , at each port was acquired at a rate of 625 Hz to calculate the pressure coefficient, $C_p = \Delta p / \frac{1}{2} \rho_\infty U_\infty^2$; here, ρ_∞ and U_∞ denote the free-stream density and velocity, respectively. The uncertainty in the C_p measurement was found

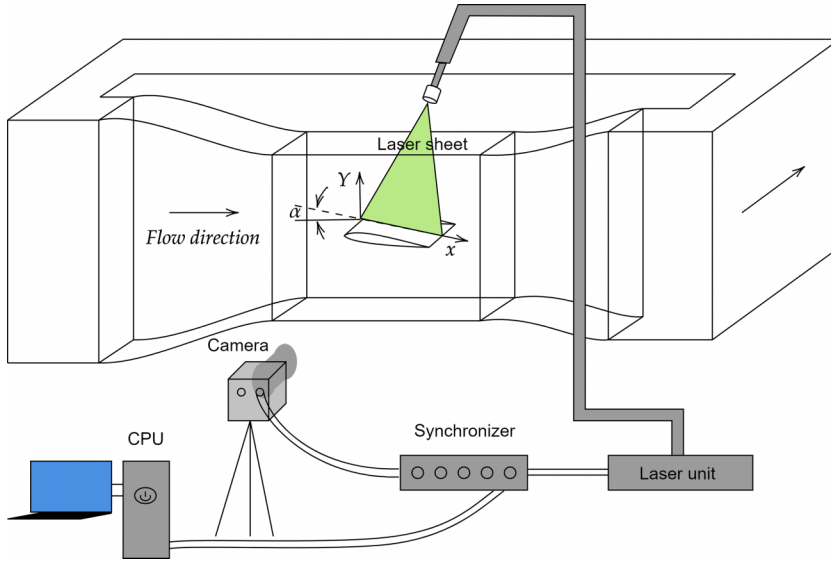


FIG. 1. A schematic diagram of the experimental setup in a close circuit wind tunnel.

to be $\pm 0.099\%$ [30]. One may refer to Siva Viknesh and Poddar [30] for further details about the aerofoil model, position of the pressure taping and the scanners.

The time-resolved particle image velocimetry (TR-PIV) measurements were carried out to study the spatiotemporal flow development over an aerofoil. Glycol-based seeding particle with a mean diameter of $1\ \mu\text{m}$ was seeded in the flow using a fog generator (SAFEX fog generator, Dantec Dynamics, Denmark). A laser light was produced from the high-frequency double pulsed Nd: YLF laser (Photonics Industries, dual head DPSS, energy 30 mJ per pulse at 527 nm at the repetition rate of 1 kHz). A laser sheet of 1-mm thickness was passed through the upper surface of the test section to illuminate the seeding particles, as schematically shown in Fig. 1. The same laser and fog generator systems were also used in the previous studies [27,35–38]. The laser sheet was aligned in the midspan plane of the aerofoil, where the measurements were carried out. A CMOS camera (Os 10-4 K camera, IDTvision, USA, resolution, 3840×2400 pixels, 9MP, with the maximum frame rate at a maximum resolution of 500 Hz at double exposure mode) and a planner lens of 100-mm focal length were used in the high-speed image acquisition. The laser and camera were synchronized using the MotionPro timing unit (IDT piv, USA).

All the measurements in the present study were carried out at a chord-based Reynolds number $Re_c = U_\infty c / \nu = 5 \times 10^4$. The free-stream velocity U_∞ in the present study is 5 m/s, which is measured at the inlet of the test section. At the same flow conditions, the free-stream turbulence (FST) level of the wind tunnel was measured without an airfoil in the test section. To measure the FST level, hotwire measurements were carried out at a sampling rate of 6 kHz for 60 s. The FST level was found to be 0.09% in the frequency band 1–1000 Hz. Surface pressure measurements were performed at several angles of attack varying within $\alpha = 0\text{--}19^\circ$. Based on the mean surface pressure measurements, the TR-PIV measurements were carried out only at four different angles of attack varying within $\alpha = 10\text{--}13^\circ$. While carrying out the TR-PIV measurements, a total of 1500 image pairs were acquired at a rate of 500 Hz. The acquired images with a correlation window of $32\ \text{pixels} \times 32\ \text{pixels}$ were then processed in a PIV processing package, ProVision XS (IDT piv, USA) to obtain the instantaneous vector fields. This processing package was also used in our earlier studies [e.g., Refs. [27,35,37–39]]. The uncertainty in the velocity measurements is mainly due to the calibration factor, the delay in the laser pulse and the particle displacement. The combined uncertainty in the velocity is found to be $\pm 1.96\%$, which was estimated following the methods

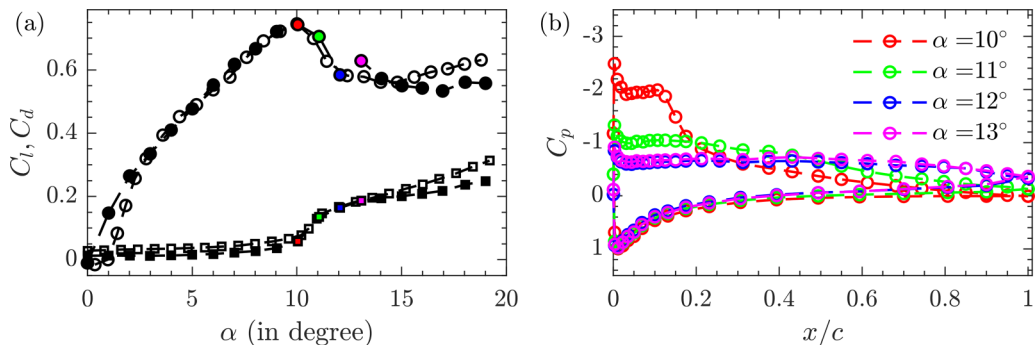


FIG. 2. (a) Variations of C_l and C_d with angle of attack, α . Description of symbols: C_l (●) and C_d (■) for the present experiment; colored symbols correspond to the selected angles of attack for which pressure distributions are shown in panel (b); C_l (○) and C_d (□) correspond the data reproduced from the study of Ohtake *et al.* [33], for comparison. (b) Variation of the mean surface pressure coefficient (C_p) for the selected α , as shown in panel (a).

reported in the literature [40–43]. In the following, U_I and U denote the instantaneous and mean velocities in the streamwise direction, respectively, whereas V_I and V denote the instantaneous and mean velocities in the wall-normal direction, respectively; the streamwise and the wall-normal fluctuating velocity components are denoted by $u(=U_I - U)$ and $v(=V_I - V)$, respectively.

III. RESULTS AND DISCUSSIONS

A. Surface pressure measurement

The normal force coefficient, C_n , and the axial force coefficient, C_a , are calculated from the C_p distribution using the conventional equations [44]: $C_n = \int_0^1 (C_{p,l} - C_{p,u}) d(\frac{x}{c})$ and $C_a = \int (C_{p,u} - C_{p,l}) d(\frac{x}{c})$. The lift coefficient, C_l , and the drag coefficient, C_d , are then calculated using the relations, $C_l = C_n \cos\alpha - C_a \sin\alpha$ and $C_d = C_n \sin\alpha + C_a \cos\alpha$. The present data of C_l and C_d are compared with the data of Ohtake *et al.* [33] at the same $Re_c = 5 \times 10^4$, as shown in Fig. 2(a). One may notice that the present data compares well with the previous study. The $C_{l,max}$ occurs at $\alpha = 10^\circ$ and is considered as the stall angle in the present study. We aim here to focus on the unsteady characteristics near the stall angle of attack. Therefore, we consider four different angles of attack (i.e., $\alpha = 10^\circ, 11^\circ, 12^\circ, 13^\circ$), marked as colored symbols in Fig. 2(a), for further investigation using the TR-PIV measurement technique. The C_p distributions for the selected angles of attack are shown in Fig. 2(b). A small constant C_p region is seen to exist in the case of $\alpha = 10^\circ$, which indicates the presence of a separated region [3,5,6]. However, a pressure drop/ pressure recovery also occurs downstream. As the α increases to 11° , C_p value drops abruptly, and the constant C_p region extends downstream, as compared to $\alpha = 10^\circ$. This sudden change in the C_p distribution is due to the short bubble burst [6]. However, the pressure recovery is still present in the case of $\alpha = 11^\circ$. A similar C_p distribution is also reported for an unsteady separation by Rinoie and Takemura [34]. Hence, it is inferred that the unsteady separation occurs at $\alpha = 11^\circ$. Further increase of the angle of attack to $\alpha = 12^\circ$ and 13° , the C_p distributions are found to be nearly flat, as compared to the case of $\alpha = 11^\circ$. This indicates that the flow is massively separated without pressure recovery. It is important to note that the boundary layer was not tripped on the pressure side (bottom surface) of an airfoil. The C_p distribution on the pressure side does not show any flat region as shown on the suction side, which implies that the flow separation is absent on the pressure side for $\alpha = 10^\circ, 11^\circ, 12^\circ$, and 13° . This is because of the high acceleration of the flow [$dC_p/d(x/c) < 0$] on the pressure side at higher α . Furthermore, the verification of the tonal noise emission is also important in the low Re_c airfoil studies. The Re_c and α considered in the present study is well beyond the limit for tonal noise generation limit proposed in the previous studies [45–48]. The details of the whole flow fields

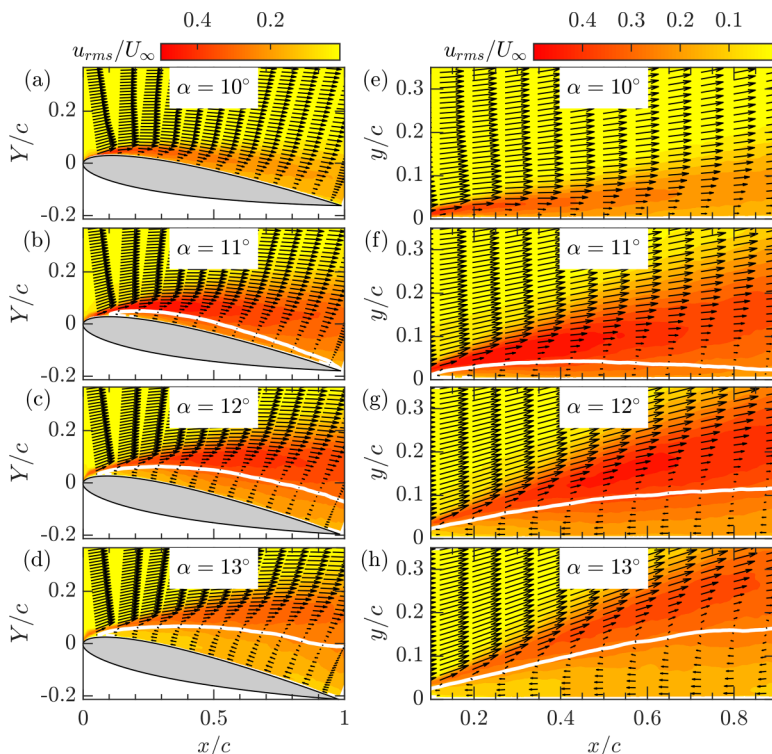


FIG. 3. Comparison of the mean flow velocity vectors overlaid with the u_{rms} contour for the fixed and surface attached coordinate systems. (a)–(d) Fixed coordinate system, and (e)–(g) Surface attached coordinate system. The white line corresponds to the zero streamwise mean velocity.

corresponding to these angles of attack, i.e., $\alpha = 10^\circ, 11^\circ, 12^\circ, 13^\circ$, as measured using the TR-PIV technique, are presented below.

B. Mean flow characteristics

Figure 3 shows the mean flow velocity vectors overlaid with the u_{rms} contours for both fixed and surface attached coordinate systems. The mesh points normal to the surface of the aerofoil were generated while the PIV images were processed in the PIV processing package, ProVision-XS. These results are shown in Figs. 3(a)–3(d), for $\alpha = 10$ – 13° . Following the works of Istvan and Yarusevych [49] and Kurelek *et al.* [50], results of these fixed coordinate systems were then converted to the surface attached coordinate system, as shown in Figs. 3(e)–3(h), for $\alpha = 10$ – 13° . In this study, the separated region is identified by the isoline of zero streamwise velocity, $U = 0$. The mean flow results in both the coordinate system show that the flow is attached at $\alpha = 10^\circ$. But, the C_p measurement shows a mild separation near the leading edge. Therefore, it is necessary to note that measuring near-wall data in PIV measurement is difficult due to surface reflection. Consequently, the mild separation could not be captured by the PIV measurement for $\alpha = 10^\circ$ case. As α increases to 11° , the flow separates significantly over a suction surface and reattaches at the trailing edge. Further increase in α resulting massive flow separation over the airfoil, leading to an open separation bubble at $\alpha = 12^\circ$ and $\alpha = 13^\circ$. This massive flow separation also extends the reverse flow region in the wall-normal direction.

Various mean flow parameters estimated for the surface attached coordinate system at different α are shown in Fig. 4. The boundary layer edge velocity, U_e , as shown in Fig. 4(a), decreases in

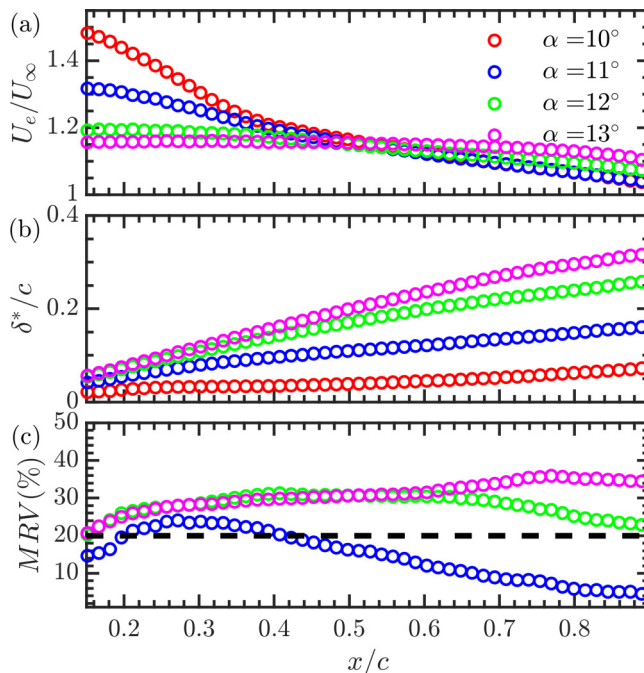


FIG. 4. Streamwise variation of the mean flow parameters at different AOA. (a) The boundary layer edge velocity variation. (b) Displacement thickness variation. (c) Maximum reverse flow velocity in percentage (considering the maximum MRV value for a corresponding chordwise position). A dashed line corresponds to the limit above which the separated shear layer becomes absolutely unstable.

the streamwise direction for $\alpha = 10^\circ$ and 11° , due to the increase in pressure gradient, but it is nearly constant throughout the upper surface of the aerofoil for $\alpha = 12^\circ$ and 13° , mainly due to the flow separation without reattachment. Figure 4(b) shows the comparison of the displacement thickness (δ^*) variation. To calculate δ^* , the experimentally measured velocity profile is first curve-fitted using smoothing spline fit to reduce the interpolation error, and then δ^* is estimated using the equation $\int_0^\delta (1 - \frac{U}{U_e}) dy$, where δ is the local boundary layer thickness. The maximum uncertainty in the estimation of the δ^* was found to be $\pm 0.94\%$. Figure 4(b) shows that δ^* increases abruptly as α increases from 10° to 11° due to the formation of a separation bubble. For further increase in α , δ^* increases due to the expansion of the separated flows in the wall-normal direction. The reverse flow intensity in a separated flow is also an important factor in the context of shear layer instability [23]. The maximum reverse flow velocity (MRV) is estimated as $-U_{\text{rev,max}}/U_e$; here, $U_{\text{rev,max}}$ denotes the maximum reverse flow velocity measured at a streamwise location. Figure 4(c) shows the MRV variation (in percentage %) for different α . A dashed line in Fig. 4(c) corresponds to the MRV = 20%, as the absolute instability takes place for 15-20% of the maximum reverse flow velocity in a separated shear layer [2,19,23,25]. The present values of the maximum reverse flow velocity satisfy the absolute instability criterion for $\alpha = 11^\circ$, 12° , and 13° .

C. Unsteady flow characteristics

One of the main unsteady flow characteristics is the flapping of the shear layer, which is associated with its vertical oscillation [15–18]. The instantaneous displacement thickness, δ_l^* , provides information about the vertical movement of a separated shear layer [25,27]. To investigate the flapping behavior of a shear layer, we estimate the instantaneous displacement thickness (δ_l^*) at $x/c = 0.3$ for different angles of attack. The maximum MRV occurs close to $x/c = 0.3$ for the

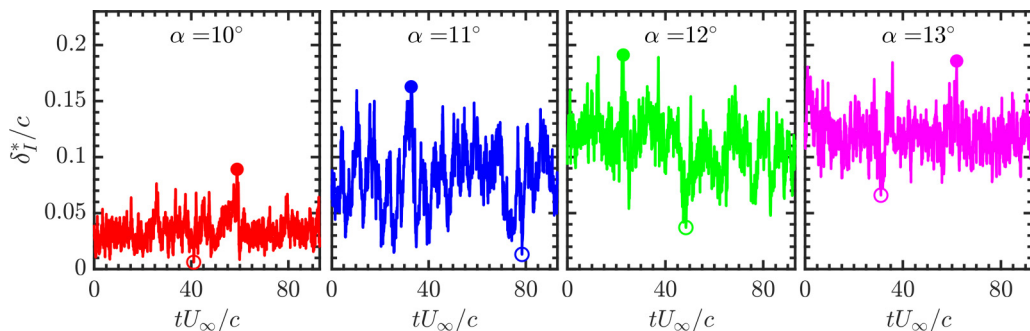


FIG. 5. Variation of the instantaneous displacement thickness at $x/c = 0.3$; open and solid symbols indicate the minimum and maximum values of the displacement thickness, respectively.

case of $\alpha = 11^\circ$. Hence, this chordwise location is considered a reference location for $\alpha = 11^\circ$, and other α cases as well for comparison purposes. The time series of δ_I^* is shown in Fig. 5; open and filled symbols denote the minimum and the maximum values of δ_I^* . The minimum displacement thickness, $\delta_{I,\min}^*$, and the maximum displacement thickness, $\delta_{I,\max}^*$, indicate the minimum and the maximum wall-normal extension of a shear layer from the wall. Therefore, Fig. 5 reveals that there exist vertical oscillations of the shear layers for all the angles of attack presented here.

The instantaneous TR-PIV realizations corresponding to $\delta_{I,\min}^*$ and $\delta_{I,\max}^*$, for different angles of attack, are shown in Fig. 6. The zero streamwise velocity, i.e., $U = 0$, lines (black lines) are also overlaid with the instantaneous vorticity contours to identify the separated regions. This figure shows that the instantaneous flow characteristics are completely different from the mean flow characteristics, as the mean flow characteristics reveal that the flow is globally separated for $\alpha = 11^\circ$, 12° , and 13° . But the instantaneous flow fields show that it is not always true at all time instants, as the flow is found to be sometimes attached, as shown in the first column of the Fig. 6. We may note that δ_I^* value changes not only due to the low-frequency oscillation of the separated shear layer but also due to the vortex shedding. Hence, the reference location of δ_I^* for the identification of global characteristics should be free from the vortex-shedding region. Hence, it is suggested to choose the reference location ahead of the onset of vortex shedding. Using the qualitative flow visualizations, Rinoie and Takemura [34] also found similar intermittent characteristics over a NACA 0012 airfoil at $\alpha = 11.5^\circ$, and they reported that this intermittent reattachment behavior occurs at a low-frequency. But in the separated phase, we also find the roller structures as shown in the zoomed-in view of the red-colored box in Fig. 6, which can be attributed to the Kelvin-Helmholtz (KH) instability of the separated shear layer [12]. The shedding of such a roller structure from a separated shear layer is a high-frequency phenomenon [51,52].

Therefore, the present quantitative observations assure that both the low-frequency and high-frequency unsteadiness play a role in the intermittent reattachment of a flow over an aerofoil. Our recent study of the separated shear layer over a flat plate reveals the presence of an intermittent vortex shedding process when $\delta_{\text{rms}}^*/\delta^* \rightarrow 0.23$ [27]. Here, δ_{rms}^* is a root-mean-squared value of δ_I^* (Fig. 5). The numerical values of the nondimensional parameter $\delta_{\text{rms}}^*/\delta^*$ are found to be 0.36, 0.36, 0.22, and 0.15 for $\alpha = 10^\circ$, 11° , 12° , and 13° , respectively. Hence, the cases for $\alpha = 10^\circ$ and 11° , $\alpha = 12^\circ$ (marginally) satisfy the intermittent vortex shedding criterion. However, $\alpha = 13^\circ$ case does not meet this intermittent vortex shedding criterion, which can be attributed to the presence of nearly regular vortex shedding, as discussed in the Appendix.

The intermittent attached and separated states are quantified by the intermittency factor (γ), which is defined here as the fraction of time during which the backflow is present at a streamwise location. Here, $\gamma = 0$ indicates the presence of forward flow in the entire measurement time, whereas 1 indicates the presence of backflow in the entire measurement time. It should be noted that the presence of backflow at a streamwise location is considered only if the backflow is present

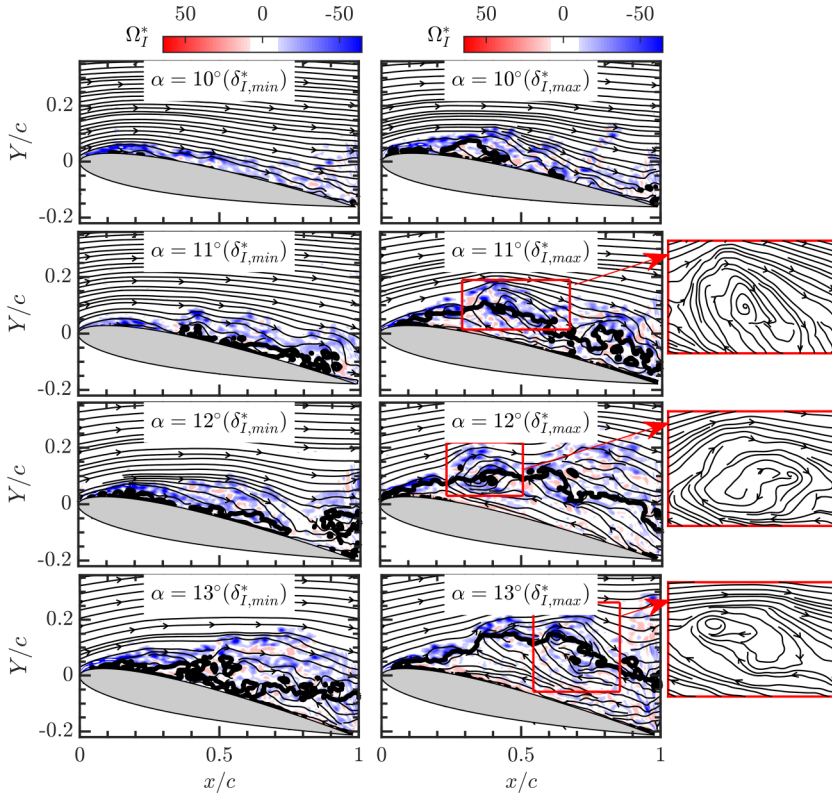


FIG. 6. Instantaneous streamlines superimposed with the instantaneous vorticity contours and the $U = 0$ line. The first column of the figure represents the realizations corresponding to the time instants marked by the open symbols in Fig. 5. The second column of the figure represents the realizations corresponding to the time instants marked by the closed symbols in Fig. 5. The roller structure is marked by a red colored box, and it is zoomed-in for better visualization.

at least in the region $0 \leq y/c \leq 0.0075$, in the intermittency calculation. The estimated γ along x/c is shown in Fig. 7. The nonzero value of γ for the case of $\alpha = 10^\circ$ indicates that the flow separation occurs instantaneously, even though the mean flow data in Fig. 3(a) shows that flow is completely attached. For the case of $\alpha = 11^\circ$, the numerical value of γ never reaches 1. This

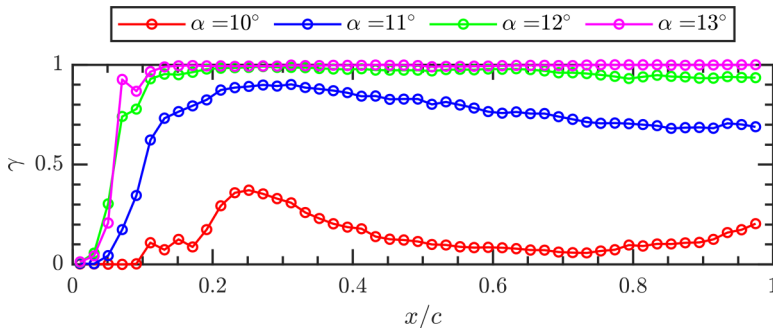


FIG. 7. Comparison of the backflow intermittency factor (γ) for $\alpha = 10^\circ$, 11° , 12° , and 13° .

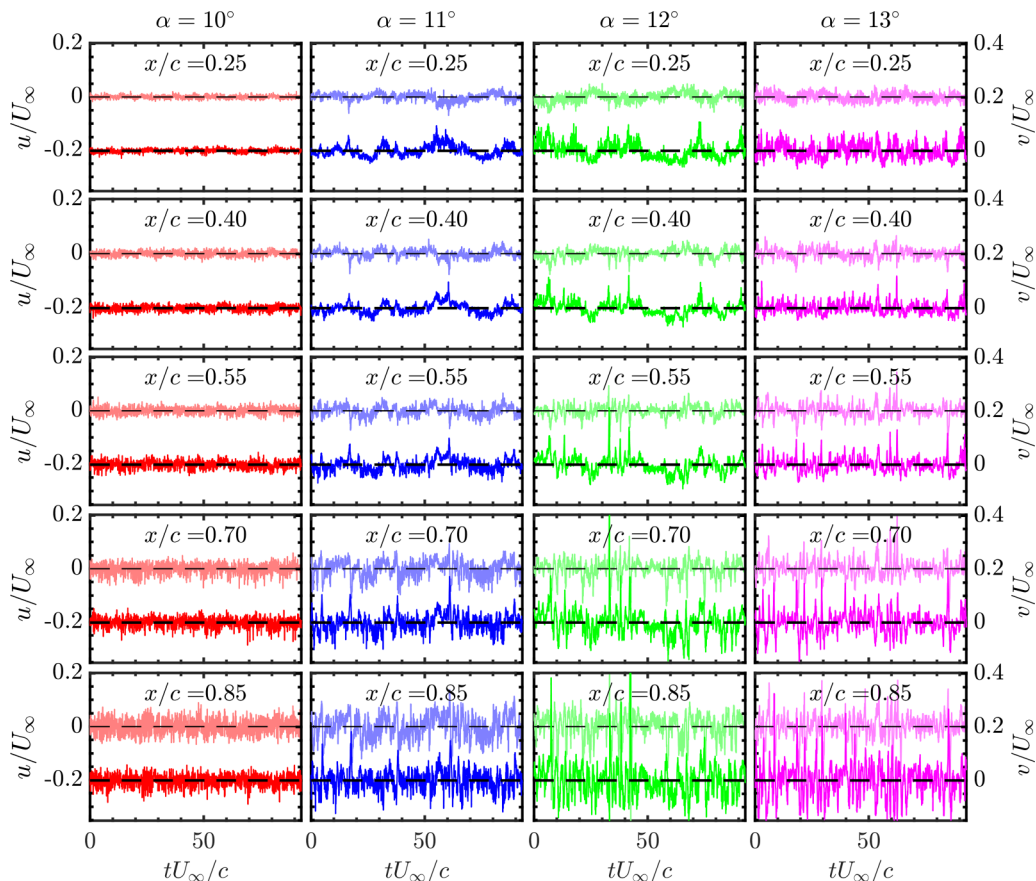


FIG. 8. Comparison of the u and v fluctuating velocity signals extracted at the wall-normal location close to $u_{\text{rms,max}}$ and $v_{\text{rms,max}}$, respectively. First and second signal in each panel from the top corresponds to the u and v fluctuating velocity, respectively. The mean value of the signal is represented by a dashed line.

implies that the flow for $\alpha = 11^\circ$ sometimes remains attached, as well, even though the mean flow [Fig. 3(b)] shows complete separation on the upper surface. Figure 7 also shows that the peak values of γ for $\alpha = 10^\circ$ and 11° occur at about $x/c = 0.25$, followed by a decrease toward the trailing edge. This indicates that the transition-to-turbulence occurs near the trailing edge, leading to an intermittent reattachment. A similar variation can also be seen for the case of $\alpha = 12^\circ$, although it is not prominent. However, we find $\gamma \approx 1$ in the major part of the upper surface, for the case of $\alpha = 13^\circ$, without a decrease toward the trailing edge after the peak value. This can be attributed to the presence of the stronger coherent vortex, which does not reattach with the wall leading to the transition-to-turbulence. However, the peak values of γ are found to be 0.37, 0.90, 0.99, and 1, for the cases of $\alpha = 10^\circ, 11^\circ, 12^\circ, 13^\circ$, respectively. The peak value is also found to occur close to the leading edge. Therefore, it reveals that the leading-edge separation is a major source of the massive intermittent separation and reattachment dynamics.

The time-series signals of the fluctuating u and v velocities at the wall-normal location close to the $u_{\text{rms,max}}$ and $v_{\text{rms,max}}$, respectively, are shown in Fig. 8 for different streamwise locations and α . One may clearly see that the amplitude of the velocity fluctuation at $x/c = 0.25$ for $\alpha = 10^\circ$ is small, as compared to the other α cases. For $\alpha = 11^\circ$ and 12° , the low-frequency oscillation is seen to be embedded with the high-frequency oscillations of the fluctuating velocity signals. The low-frequency oscillation is observed in both the u and v fluctuating velocity signals, for

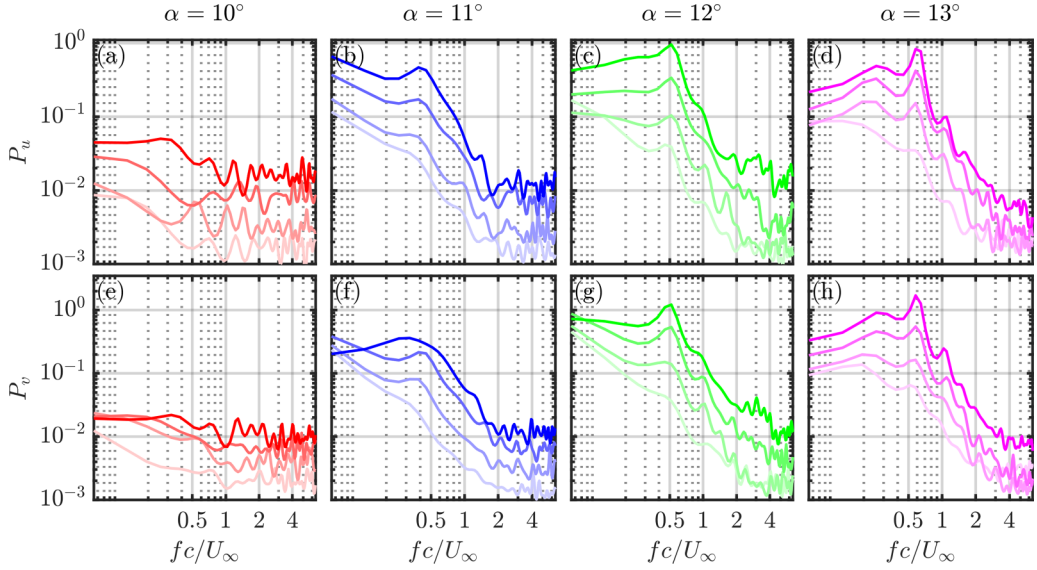


FIG. 9. Comparison of the power spectra of the u and v fluctuating velocity signals shown in Fig. 8 at different streamwise locations. (a)–(d) For u fluctuating velocity signal. (e)–(h) For v fluctuating velocity signals. Four power spectrum curves (from bottom to top) correspond to the streamwise locations $x/c = 0.40, 0.55, 0.70,$ and 0.85 .

$\alpha = 11^\circ$ and 12° . However, as the streamwise distance increases, the low-frequency oscillation is seen to diminish, and the high-frequency oscillation is found to dominate the fluctuating velocity signals (see signals at $x/c = 0.85$), for $\alpha = 11^\circ$ and 12° . The low-frequency oscillation at the initial streamwise locations is due to the vertical oscillation of the separated shear layers. For $\alpha = 13^\circ$, the low-frequency oscillation is not prominent as compared to the $\alpha = 11^\circ$ and 12° cases. This can be attributed to the continuous vortex shedding for $\alpha = 13^\circ$.

Figure 9 shows the power spectra of the fluctuating velocity signals that are shown in Fig. 8 at $x/c = 0.4, 0.55, 0.70, 0.85$, for all the α cases; the power spectra were estimated using the maximum entropy method [53]. One may clearly notice in Fig. 9 that the spectral energy at $x/c = 0.4$ is distributed at the low-frequency range for all the angles of attack, whereas the clear peaks can be seen in the power spectra for further downstream locations except for $\alpha = 10^\circ$. Moreover, the spectral content in the low-frequency band increases with x/c . This is due to the flapping of the separated shear, which oscillates in both the vertical and streamwise directions. In other words, it is subjected to contraction and expansion over an airfoil surface. The resulting streamwise oscillation increases the spectral content with x/c in the low-frequency range. A similar observation is also reported in the study of turbulent separation bubble [10], where it is called the breathing motion of the separation bubble. The peak in the frequency spectra is mainly due to the vortex shedding from the airfoil. Hence, the spectrum for $\alpha = 10^\circ$ indicates that the vortex shedding is very weak, which was further confirmed by visualizing the instantaneous TR-PIV realizations. The power spectra of the u and v fluctuating velocities reveal that although the vortex shedding frequency at a particular α does not change significantly with downstream distance, it does change with α . This may be attributed to the viscous effect on the vortex shedding. The viscous effect on the vortex shedding may decrease due to an increase in the shear layer height at a higher α , which may lead to an increase in the shedding frequency [54]. The nondimensional peaks (fc/U_∞) are found to be at 0.45, 0.5, and 0.6 for $\alpha = 11^\circ, 12^\circ, 13^\circ$, respectively. In their direct numerical simulation (DNS) for the flow over a NACA-0012 airfoil, Rodríguez *et al.* [55] found the vortex shedding frequency (fc/U_∞) to be 0.6 at $\alpha = 12^\circ$ for $Re_c = 5 \times 10^4$; this value is comparable with the present experimental value

at $\alpha = 12^\circ$. Although the above local unsteady characteristics of the flow reveal the presence of low and high-frequency oscillations, it is also important to investigate the unsteady global characteristics of the flow. Therefore, the POD analysis of the TRPIV data has been carried out to shed light on the unsteady global characteristics of the flow for different α considered here.

D. POD analysis

The proper orthogonal decomposition (POD) analysis of a flow field can provide several spatial modes, which are ranked based on the level of energy. These modes often facilitate a clear understanding of complex flow dynamics. Using this analysis, the fluctuating velocity field can be decomposed as

$$\mathbf{v}'(\mathbf{x}, t_n) = \sum_k a^k(t_n) \Phi^k(\mathbf{x}), \quad (1)$$

where $\mathbf{v}'(\mathbf{x}, t_n)$ is the fluctuating flow field; $\Phi^k(\mathbf{x})$ and $a^k(t_n)$ are the k^{th} spatial POD mode shape and its time coefficient, respectively. Here, the fluctuating flow field consists of u and v components. The POD mode shapes and their time coefficients are estimated using the method of snapshot [56]. The POD methodology, as detailed in our previous works [27,38,57], is briefly outlined here. The u and v fluctuating velocity components are arranged in a matrix, A . The autocovariance matrix, $C(=A^T A)$, is determined from the matrix A . The eigenvalues, λ_k , and their corresponding eigenvectors, ϕ^k , are determined from the autocovariance matrix, C . The eigenvectors are arranged based on their energy level (eigenvalues). The eigenmodes/POD modes (Φ^k) are determined from the following relation,

$$\Phi^k = \sum_{i=1}^M \phi_i^k \mathbf{v}'_i, \quad (2)$$

where M is the number of snapshots/PIV realizations. The normalized basis functions are obtained such that $(\Phi^k, \Phi^n) = \delta_{mn}$, where δ_{mn} is the Kronecker δ . The time coefficient, a^k , of the POD modes are calculated from the inner product of normalized Φ^k and \mathbf{v}' ,

$$a^k = (\mathbf{v}', \Phi^k). \quad (3)$$

The relative energy, E_r , of the POD modes is calculated as

$$E_r = \frac{\lambda_r}{\sum_{r=1}^M \lambda_r} \times 100\%. \quad (4)$$

The cumulative energy, E_c , of the POD modes is calculated as

$$E_c = \frac{\sum_{r=1}^c \lambda_r}{\sum_{r=1}^M \lambda_r} \times 100\%. \quad (5)$$

The relative and cumulative energies, associated with various modes, are shown in Fig. 10. The first 20 modes contribute $\gtrsim 60\%$ of the flow energy. This indicates a low-dimensional nature of the separated flow under consideration. However, Fig. 10 also shows that the relative energies of the first and second modes are not equal, that is, the eigenvalues of the first and second modes are not degenerate. This implies that it is not associated with the vortex shedding. Similar observations for the case of a separated shear layer are also reported in the literature [10,15,27,58,59]. While Michelis *et al.* [15], who studied a separated shear layer subjected to an impulsive forcing, reported that the first mode is due to the flapping motion of the shear layer, whereas others [e.g., Refs. [10,58,59]] reported that the first POD mode is due to the low-frequency unsteadiness. However, in the present study, we find that the relative energy (E_r) of the first mode increases for $\alpha = 11^\circ$ and 12° (see Fig. 10), and then it decreases for $\alpha = 13^\circ$. This indicates that the amplitude of the low-frequency oscillation first increases and then reduces with an increasing angle of attack. The present experimental observation is consistent with the recent observation of Eljack *et al.* [2], who numerically simulated a flow over

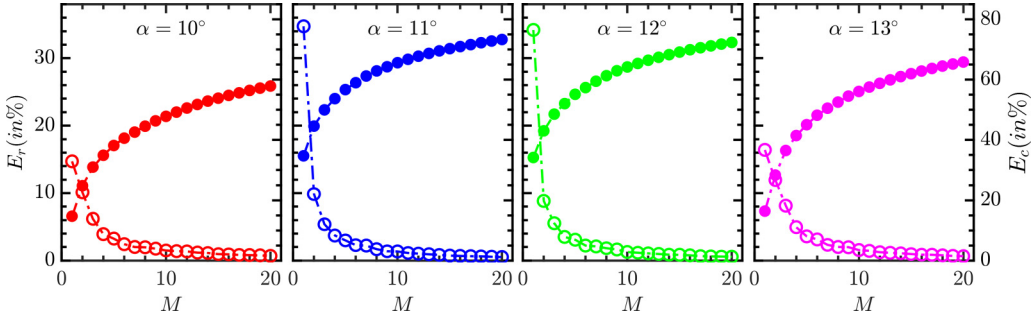


FIG. 10. Variations of the relative and cumulative energy levels of the POD modes (i.e., the uv -POD modes) for $\alpha = 10^\circ, 11^\circ, 12^\circ,$ and 13° . Open symbols correspond to the relative energy (E_r) level, and closed symbols correspond to the cumulative energy (E_c) level.

a NACA-0012 airfoil and found that the amplitude of low-frequency oscillation increases and then decreases with α .

The POD mode shapes are also calculated to identify the spatial structure associated with the low- and high-frequency unsteadiness in the flow. The first six dominant POD modes are shown in Fig. 11, for various α . Contours of the wall-normal component of the POD modes have been superimposed with the vector plot of a POD mode. One can notice that there is no considerable ϕ_v component in the first mode for $\alpha = 10^\circ, 11^\circ,$ and 12° ; here, ϕ_v indicates the wall-normal component of a POD mode. This shows that the vortical structure is absent. However, presence of a small vortical structure can be observed for $\alpha = 13^\circ$. This is because of the fact that the flow does not have sufficient momentum to reattach due to the high adverse pressure gradient. The instantaneous flow field for $\alpha = 13^\circ$, as displayed in Fig. 6, also shows flow separation near the trailing edge, even at $\delta_{l,\min}^*$. On the other hand, the vortical structures are found to be absent in the first two modes for $\alpha = 10^\circ$ as the flow has sufficient momentum at $\alpha = 10^\circ$. However, the vortical structures are found to be present from the third POD mode onward for all the cases. The mode shapes in Fig. 11 also show that the location and sizes of the vortical structure change with the higher-order POD modes (see $M = 3-6$ for all the cases), indicating their intermittent formation.

To find the unsteady characteristics associated with the POD modes, the time coefficients (a_1-a_6) corresponding to the first six dominant POD modes are shown in Fig. 12, for all the cases. Figure 12 shows that the unsteadiness at $\alpha = 10^\circ$ is relatively small, as compared to the other cases, i.e., $\alpha = 11^\circ, 12^\circ,$ and 13° . This is because of the fact that the flow at $\alpha = 10^\circ$ is attached for the longer time duration (see Fig. 7), and therefore, the amplitude of fluctuation is small for $\alpha = 10^\circ$. This is also consistent with Fig. 10. As α increases to 11° , the time coefficient of the first POD mode, a_1 , clearly shows the low-frequency oscillation. The amplitude of this low-frequency oscillation is visibly higher than that for $\alpha = 10^\circ$. This high-amplitude low-frequency oscillation indicates intense intermittent separation-reattachment of the flow, as is also seen for $\alpha = 12^\circ$. However, further increase in α to 13° , the amplitude of the oscillation decreases (see a_1 for $\alpha = 13^\circ$), which is also consistent with Fig. 10. This low-frequency oscillation reduces for the higher order modes for $\alpha = 11^\circ, 12^\circ, 13^\circ$ (see time series for a_2-a_6), and the high-frequency oscillation emerges due to the shedding of the vortical structure.

Further, Fig. 13 shows the power spectra for the time coefficients. For all the cases of the first mode, the maximum energy is seen to be distributed over the lower frequency range. This is attributed to the low-frequency oscillation of the separated shear layers, as discussed earlier. Even though the high-frequency oscillation appeared in the time-coefficients for the Modes $M > 1$, it will not necessarily represent the vortex shedding mode. The vortex shedding modes are identified using the v -POD analysis as detailed in the Appendix. We find that $M-5, M-4, M-3,$ and $M-3$ are the vortex shedding modes for the cases of $\alpha = 10^\circ, 11^\circ, 12^\circ, 13^\circ$, respectively. This implies that

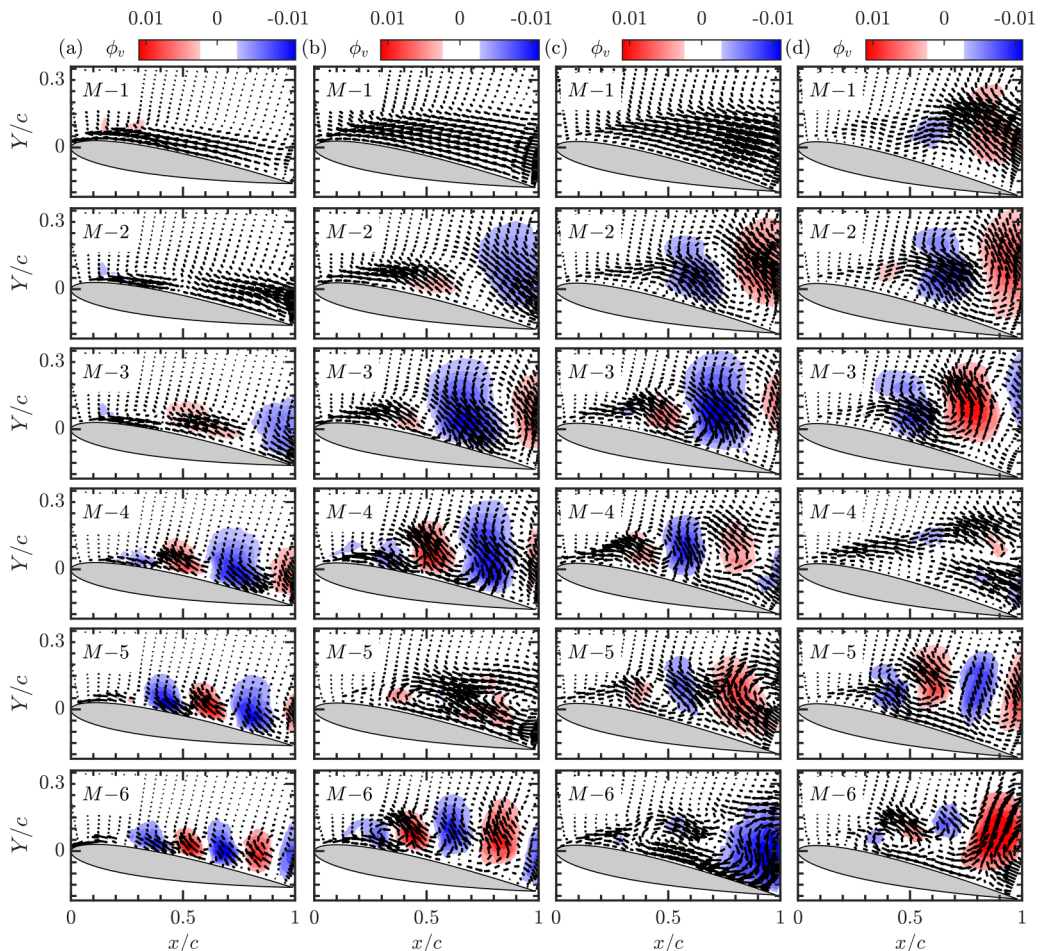


FIG. 11. Two-component POD modes (i.e., the uv -POD modes) superimposed with the contours of its wall-normal component (i.e., ϕ_w). (a) $\alpha = 10^\circ$, (b) $\alpha = 11^\circ$, (c) $\alpha = 12^\circ$, (d) $\alpha = 13^\circ$.

the modes in between the first mode and the vortex-shedding mode (e.g., $M-2$, $M-3$, and $M-4$ for $\alpha = 10^\circ$) can be attributed to the interaction of the low-frequency and the vortex-shedding mode.

The above POD analysis reveals that the first POD mode is associated with the low-frequency dynamics of the flow. The amplitude of the low-frequency oscillation initially increases (till $\alpha = 12^\circ$) and then reduces ($\alpha = 13^\circ$). The present experimental observation supports the numerical results of Eljack *et al.* [2].

E. Separation and reattachment mechanisms

Here, we investigate the instantaneous flow fields to understand how the flow goes from the attached state to the separated state and/or from the separated state to the attached state. We find that the flow is in the attached state when δ_l^* reaches its minimum value, and the flow goes to a completely separated state when δ_l^* reaches its maximum value (see Fig. 6, for $\alpha = 11^\circ$ and $\alpha = 12^\circ$). It should be noted here that the separated and attached states at the maximum and minimum values of δ_l^* , respectively, may not be general, as it may change, if the flow conditions, such as Re_c , FST level, etc., change. However, it is found to hold good for the present separated cases. To shed light on the separation and reattachment mechanisms, we choose one oscillation cycle

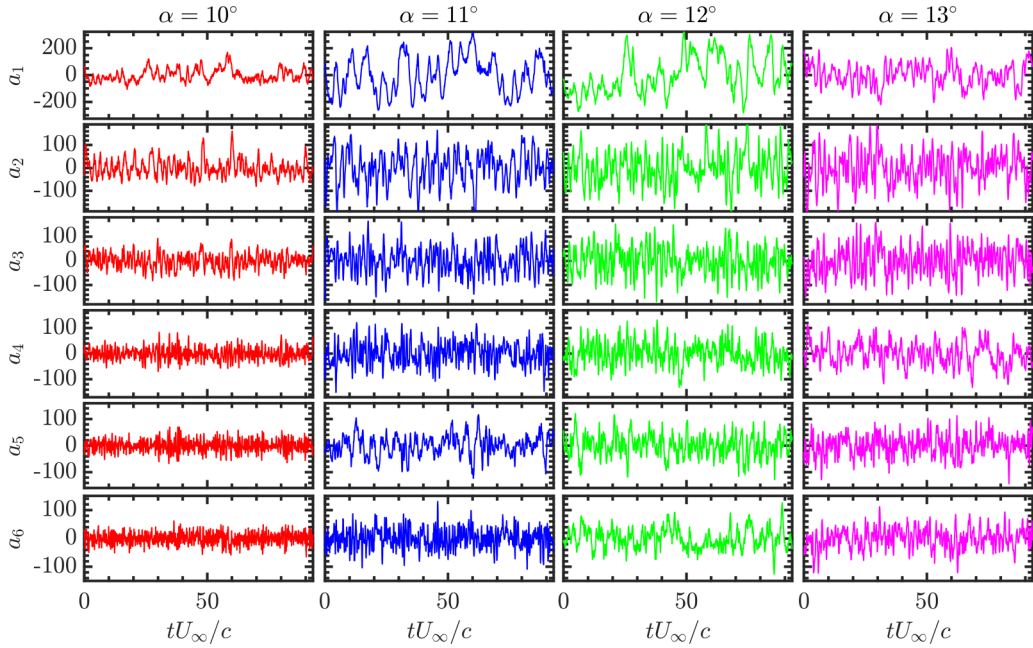


FIG. 12. Comparison of the time coefficients of the first six POD modes for $\alpha = 10^\circ, 11^\circ, 12^\circ, 13^\circ$.

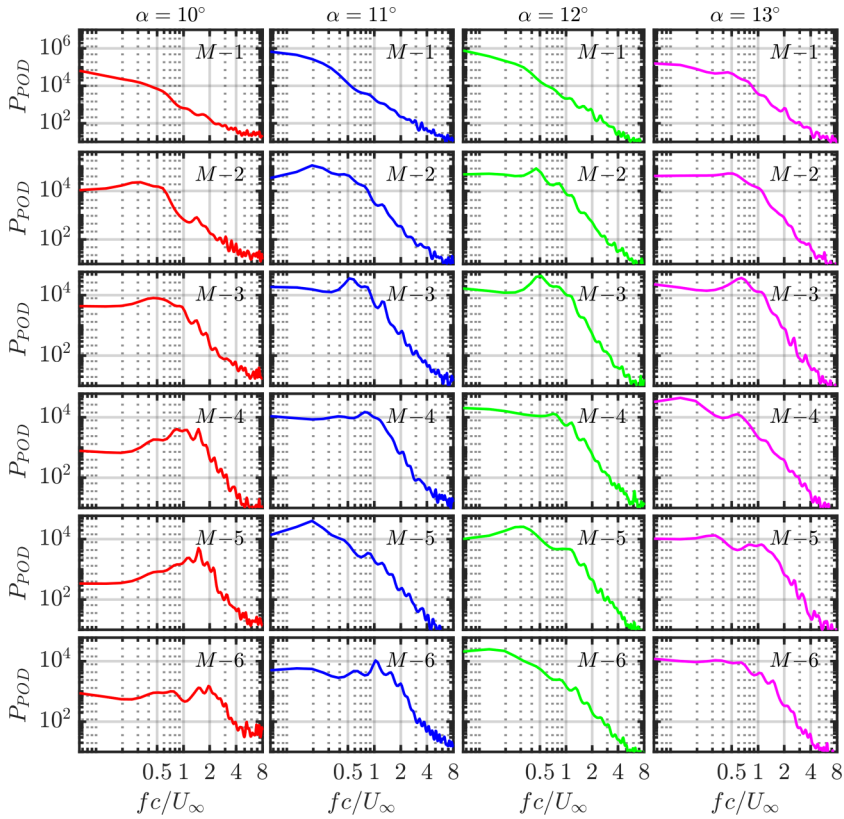


FIG. 13. Comparison of the frequency spectra of the first six POD modes for $\alpha = 10^\circ, 11^\circ, 12^\circ, 13^\circ$.

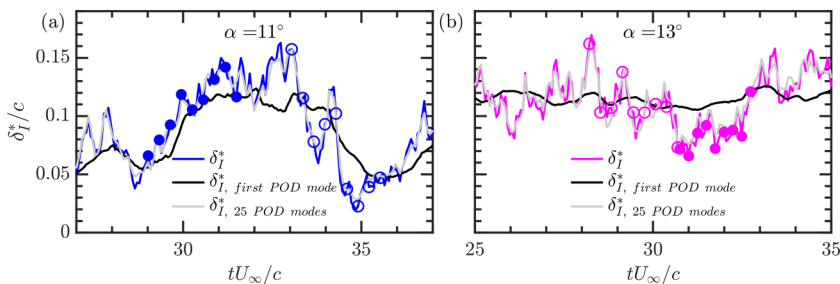


FIG. 14. One oscillation cycle of the δ_I^* from the Fig. 5, along with the δ_I^* estimated from the reconstructed POD modes for the cases of $\alpha = 11^\circ$ and $\alpha = 13^\circ$. Filled and open symbols correspond to the selected frames for further investigation on increasing and decreasing δ_I^* curve, respectively.

of δ_I^* for $\alpha = 11^\circ$, as shown in Fig. 14(a). One such similar oscillation cycle for $\alpha = 13^\circ$ is also shown in Fig. 14(b) to investigate how the amplitude of the low-frequency oscillation decreases as compared to the cases for $\alpha = 11^\circ$ and $\alpha = 12^\circ$. Moreover, $\delta_{I, \text{first POD mode}}^*$ and $\delta_{I, 25 \text{ POD modes}}^*$, which are instantaneous displacement thicknesses estimated from the reconstructed velocity fields using the first POD mode and the first 25 POD modes, respectively, are also superimposed with δ_I^* . One can clearly see that the $\delta_{I, \text{first POD mode}}^*$ is associated with the low-frequency oscillation, as shown in Figs. 14(a) and 14(b). Further, the amplitude of the low-frequency oscillation is seen to decrease for the case of $\alpha = 13^\circ$, as compared to the case of $\alpha = 11^\circ$. However, $\delta_{I, 25 \text{ POD modes}}^*$ matches well with the δ_I^* , which indicates that the reconstructed velocity field with the first 25 POD modes is good enough to capture the flow dynamics satisfactorily.

The instantaneous streamlines at some time instants corresponding to increasing and decreasing δ_I^* are shown in Figs. 15(a) and 15(c), respectively. The contour line corresponding to $U = 0$ is also superimposed with the streamlines to identify the separation and reattachment. These instantaneous figures clearly show the progress of a nearly attached state to a separated state or a separated state to a nearly attached state of the flow, along with some vortical structures. However, to make it more clear, the instantaneous flow fields, as shown in Figs. 15(a) and 15(c), are reconstructed using 25 POD modes, and the corresponding streamlines are shown in Figs. 15(b) and 15(d), respectively. The contour line corresponding to $U = 0$ in these reconstructed figures is obtained from a reconstructed velocity field based on the first POD mode alone, as the first POD mode is associated with the low-frequency oscillation of the shear layer. In a similar way, Mohammed-Taifour and Weiss [10] identified a breathing motion of the turbulent separation bubble using the first POD mode reconstruction. However, these reconstructed $U = 0$ contour lines and the reconstructed streamlines now clearly show the separations and the vortical motions as compared to the instantaneous flow fields in Figs. 15(a) and 15(c). It should be noted that the correspondences between the vortical structure identified by the reconstructed closed streamlines and the reconstructed vorticity were ensured; however, this has not been shown here for brevity.

Figure 15(b) clearly displays how a small separated region goes to the fully separated state. At time instant $6\Delta t$, a small vortex at about $x/c = 0.5$ is seen to enlarge both in the streamwise and wall-normal directions, as compared to the time instant at $1\Delta t$. This vortex pumps the fluid upstream, leading to an increase in the height of the shear layer. As a result, the shear layer becomes unstable, resulting in another vortex at $11\Delta t$ time instant. As time progresses, the separated region further extends in both the streamwise and wall-normal directions. Eventually, the separated region reaches the trailing edge and forms an open bubble [see Fig. 15(b) at $21\Delta t$]. Subsequently, the larger vortical structures form and convect downstream, as seen in the subsequent time instants ($26-41\Delta t$) in Fig. 15(b). The streamlines show that the vortical structure pumps fluids upstream. Therefore, comparing Figs. 14(a) and 15(b), it can be interpreted that the height of the shear layer increases due to the backflow pumped by the downstream vortical structure. Now, the question arises of how

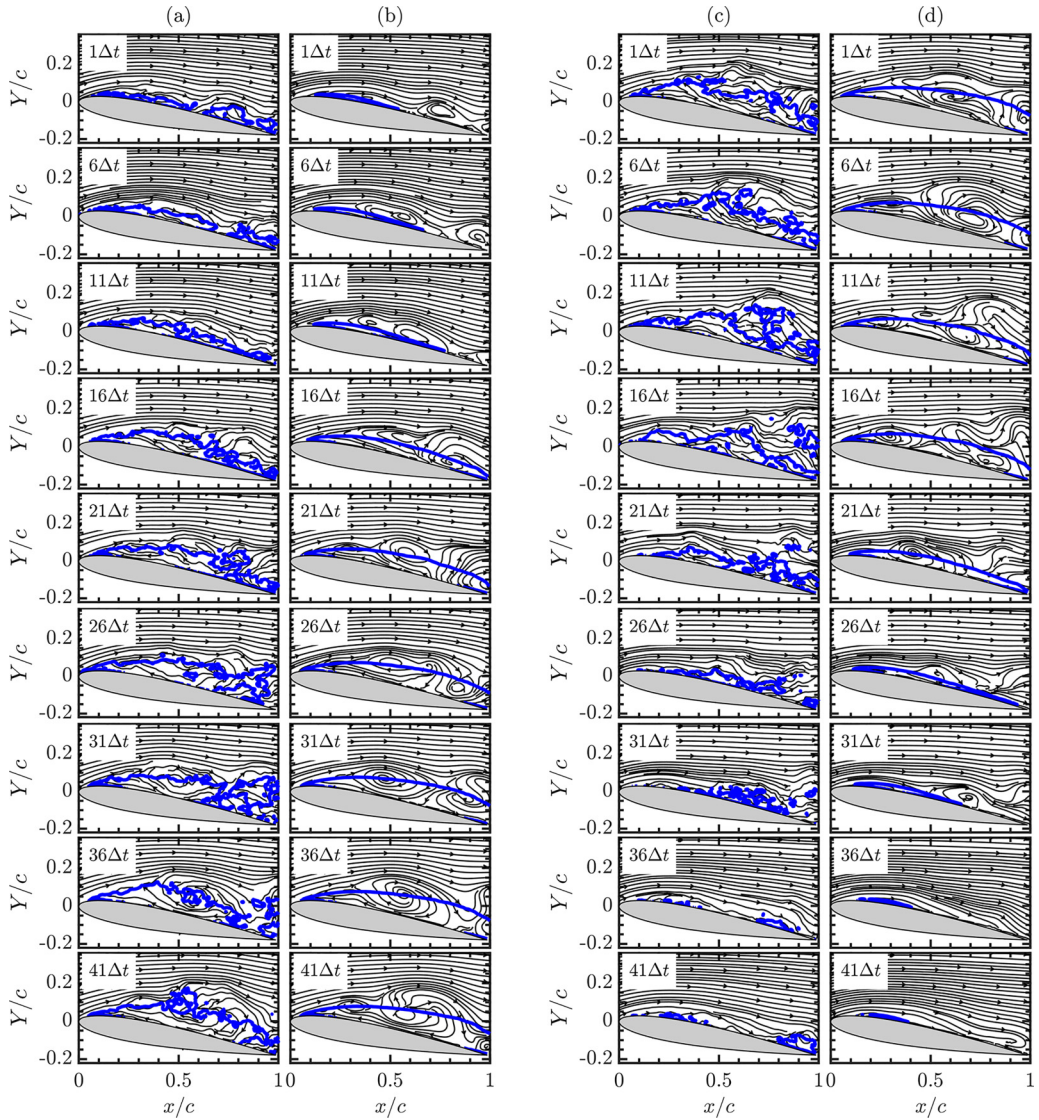


FIG. 15. Comparison of the instantaneous and the reconstructed streamlines using first 25 POD modes for the case of $\alpha = 11^\circ$. (a), (b) Instantaneous and its reconstructed streamlines corresponding to the time instants shown by filled symbols in Fig. 14(a). (c), (d) Instantaneous and its reconstructed streamlines corresponding to the time instants shown by open symbols in Fig. 14(a). Description of blue line: (a), (c) the isoline of $U = 0$ estimated from the instantaneous velocity field; (b), (d) the isoline of $U = 0$ estimated from the reconstructed velocity field using first POD mode.

this backflow pumping mechanism is stopped and whether this mechanism also plays a role in the reattachment process.

The time sequence in Fig. 15(d) displays how the flow goes to the reattachment state from the completely separated state. At time instant $1\Delta t$, a vortical structure, which can clearly be seen in Fig. 15(d), pumps the fluid upstream. As time progresses, this vortical structure gets distorted while it convects downstream, as seen in Fig. 15(d) at $11\Delta t$ time instant. This distortion of the vortical structure may be attributed to the secondary instability of the separated shear layer [26].

Here, secondary instability refers to the instability in the shed vortices. This instability in the shed vortices occurs mainly due to the spanwise deformation of the vortex core (elliptical instability) and the penetration of the three-dimensional disturbances from the braid region (hyperbolic instability) to the main vortex region [26]. The loss of coherent pattern/severe distortion of the vortex due to the secondary instability may depend on the level of spanwise deformation and the strength of the three dimensional disturbances entering into the main vortex region. At time instant $11\Delta t$, this level might be high, leading to incoherent pattern/severe distortion. However, further investigation is necessary to confirm this aspect. Due to the distortion of the vortical structure, the supply of the backflow to the upstream reduces, leading to the reduction in the height of the shear layer, as can be seen in Fig. 15(d) at $21\Delta t$ time instant. The reduction in the shear layer height increases the viscous effect leading to further contraction of the separated region, as seen at $31\Delta t$ instant. As time progresses further, the vortical structure completely disappears, leading the major part of the flow to the attached state, as seen at $41\Delta t$ time instant.

The time sequence in Fig. 16 demonstrates how the amplitude of the low-frequency oscillation decreases as α increases to 13° . Figures 16(a) and 16(b) show the instantaneous and reconstructed streamlines, respectively, corresponding to the time instants at which δ_l^* decrease [Fig. 14(b)]. Similarly, Figs. 16(c) and 16(d) show the instantaneous and reconstructed streamlines, respectively, corresponding to the time instants at which δ_l^* increases [Fig. 14(b)]. It should be noted that the flow field was reconstructed using the first 25 energetic POD modes, as was done for $\alpha = 11^\circ$. The instantaneous $U = 0$ line is superimposed with the instantaneous streamlines, whereas the contour line corresponding to $U = 0$ in the reconstructed figures is obtained from a reconstructed velocity field based on the first POD mode alone and it is also superimposed with the reconstructed streamlines, as shown in Figs. 16(b) and 16(d). These reconstructed figures clearly show the separation and the vortical structures, as compared to the instantaneous streamlines.

Figure 16(b) at $1\Delta t$ time instant clearly shows that the flow is fully separated and the vortical structures are well organized. As time progresses, these vortical structures convect downstream. In the process, the supply of the backflow in the upstream direction reduces, leading to a reduction in the height of the shear layer [see the reconstructed panel at $11\Delta t$ time instant in Fig. 16(b)]. Nevertheless, the separated flow continues to exist due to the next developing vortex near the leading edge [see the reconstructed panel at $11\Delta t$ time instant in Fig. 16(b)]. This vortex does not grow in size but gets distorted and loses its coherent pattern (see the reconstructed panel at $41\Delta t$ time instant). As a result, the supply of the backflow in the upstream direction decreases, as seen in the reconstructed panel at $41\Delta t$ in 16(b). Although the vortical structure gets distorted and loses its coherent pattern, the flow does not go to the attached state, as was observed for the case of $\alpha = 11^\circ$ [see Fig. 15(d)]. On the contrary, the shear layer height increases as time progresses, as shown in Fig. 14. The streamlines in Fig. 16(d) show how the flow develops in the subsequent time instants. A small vortical structure near the leading edge grows with time, as seen in the reconstructed panels at $1-9\Delta t$ time instants in Fig. 16(d). In the process, the shear height increases, eventually leading to another vortical structure at $13\Delta t$ instant. Similar vortical structures were also observed in the process of increasing δ_l^* for $\alpha = 11^\circ$, as seen in the reconstructed panels at $1-9\Delta t$ time instants in Fig. 15(b). As time progresses, the supply of the backflow in the upstream direction increases, which leads to the generation of a stronger vortical structure [see the reconstructed panel at $33\Delta t$ time instant in Fig. 16(d)].

Therefore, the reduction in the amplitude of the low-frequency oscillation for the case of $\alpha = 13^\circ$ can mainly be attributed to the supply of continuous backflow to the upstream direction from the downstream vortical structures, as compared to the case of $\alpha = 11^\circ$. The reduction in low-frequency oscillation is associated with the reduced oscillation in the shear layer height, which is similar to the mechanism of mean flow deformation, as detailed in Marxen and Henningson [26]. However, the main source for the flow deformation in the present study and in the study of Marxen and Rist [60] are internally varying backflow due to the downstream vortical structure and the externally imposed disturbance, respectively. Moreover, it was found that a minimum amount of disturbance is necessary to maintain the bubble in a short bubble state/vortex shedding state. Otherwise, the

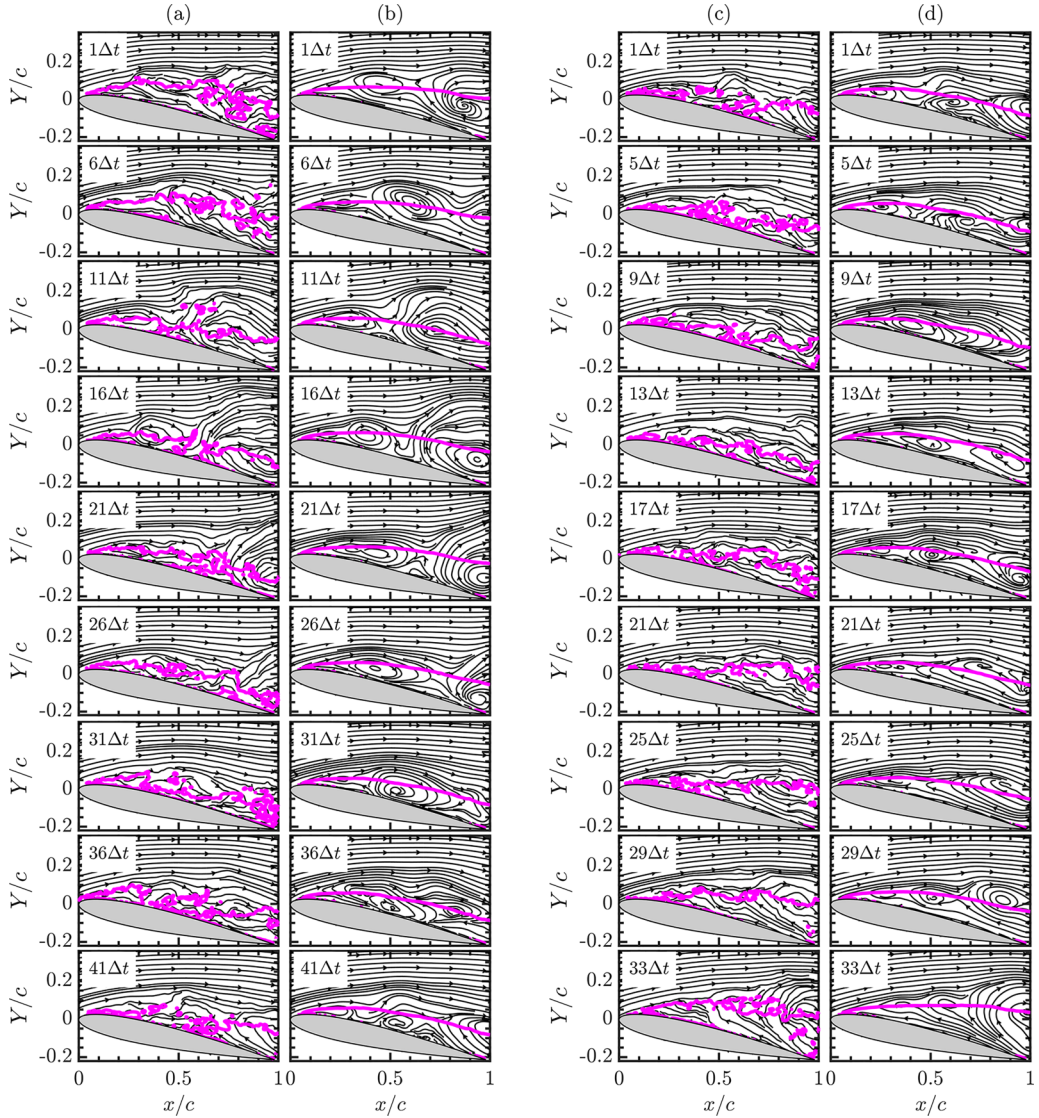


FIG. 16. Comparison of the instantaneous and its reconstructed streamlines using first 25 POD modes for the case of $\alpha = 13^\circ$. (a), (b) Instantaneous and its reconstructed streamlines corresponding to the time instants shown by open symbols in Fig. 14(b). (c), (d) Instantaneous and its reconstructed streamlines corresponding to the time instants shown by filled symbols in Fig. 14(b). Description of blue line: (a), (c) the isoline of $U = 0$ estimated from the instantaneous velocity field; (b), (d) the isoline of $U = 0$ estimated from the reconstructed velocity field using first POD mode.

bubble goes to a long bubble state with the absence of vortex shedding signature [see Ref. [26]], which is called a bursting state. In contrast, the present study shows the vortex shedding even in the long bubble state (completely separated state). Similar to the present study, the vortex-shedding signature in the long bubble without any external disturbance (i.e., at 0% FST) is also observed in some previous studies [e.g., Refs. [53,59]]. The discrepancy, that is, the presence of vortex shedding in the present work and the absence of vortex shedding/bursting in the work of Marxen and Rist [60] for a long bubble, may be due to the different base flow states for which the stability characteristics

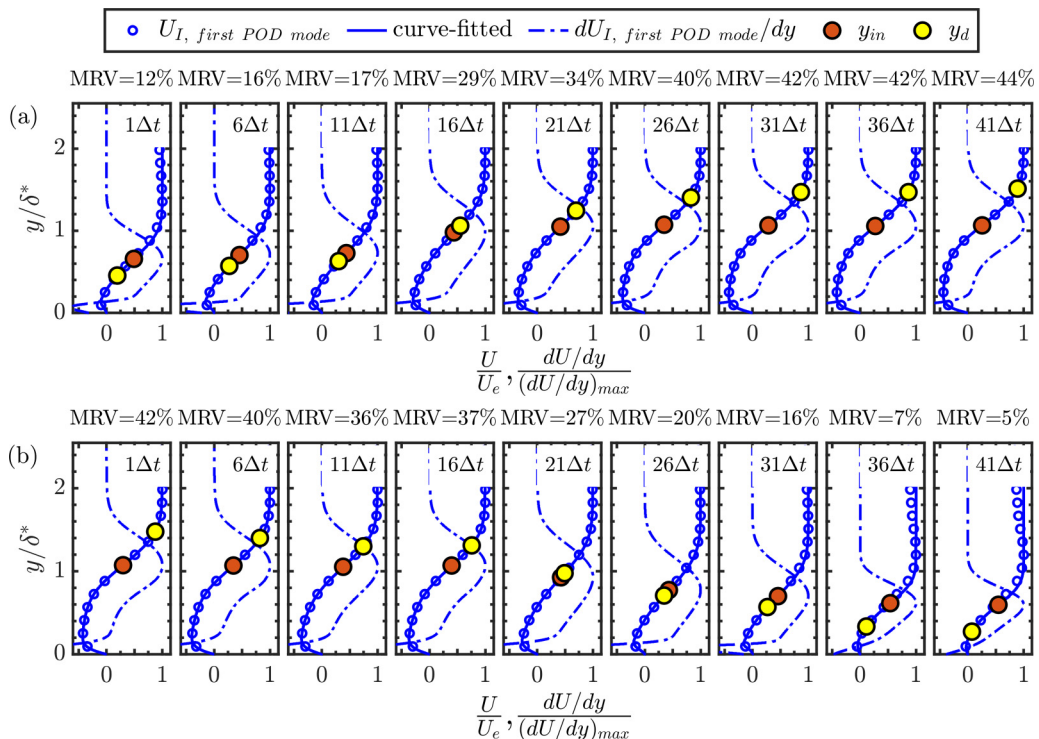


FIG. 17. Variation of the reconstructed instantaneous velocity profiles extracted at $x/c = 0.3$, using the first POD mode, for $\alpha = 11^\circ$. (a) Reconstructed velocity profiles that correspond to TR-PIV realizations shown in Fig. 15(a). (b) Reconstructed velocity profiles that correspond to TR-PIV realizations shown in Fig. 15(c).

may be different. This implies that the absence of the vortex shedding from a long bubble (or bubble bursting) may not solely depend on the minimum amount of disturbance amplitude but also on the influence of the other parameters, such as the distance between the point of inflection from the wall, amount of reverse flow, etc. Therefore, we investigate the change of shape of the velocity profiles and their stability characteristics in the following sections.

F. Instantaneous velocity profiles during the low-frequency oscillation

It is interesting to investigate the instantaneous velocity profiles while the separated shear layer is subjected to low-frequency oscillation, as these profiles may be associated with the inflectional instability leading to intermittent vortex shedding. From the analyses in Secs. III D and III E, we find that the first POD mode is associated with low-frequency oscillation. Hence, the reconstructed velocity profiles using the first POD mode at $x/c = 0.3$ are displayed in Fig. 17(a), corresponding to the time instants shown in Fig. 15(a). The points of inflection (y_{in}) are also shown in Fig. 17(a); it should be noted here that these points are estimated following Nishioka *et al.* [61] from the curve-fitted velocity profiles to avoid errors due to the numerical differentiation. Figure 17(a) shows the variations in the velocity profiles when the flow goes from an attached state to a completely separated state. Similarly, Fig. 17(b) shows the variations in the velocity profiles when the flow goes from a completely separated state to an attached state.

While a separated flow changes from an attached state to a completely separated state, one can clearly see that the heights of the inflection points and the mean dividing streamlines (y_d) from the wall increase with time as can be seen in Fig. 17(a). This leads the flow to be unstable via the inflectional instability mechanism. Consequently, a vortical structure originates due to the shear

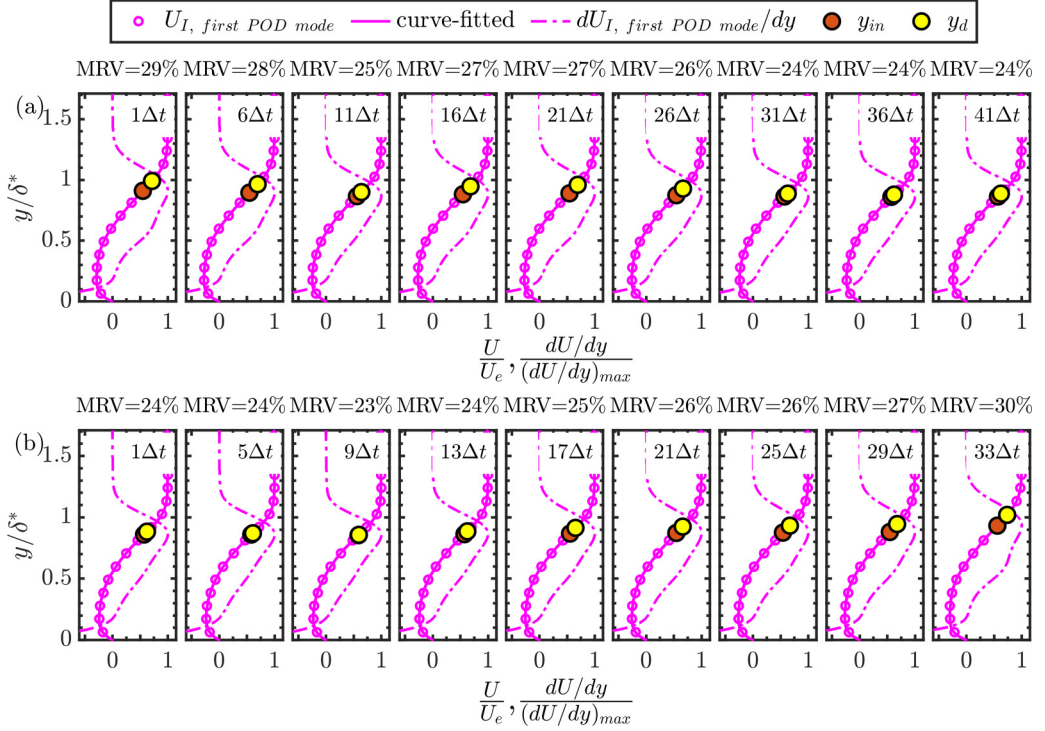


FIG. 18. Variation of the reconstructed instantaneous velocity profiles extracted at $x/c = 0.3$, using the first POD mode, for $\alpha = 13^\circ$. (a) Reconstructed velocity profiles that correspond to TR-PIV realizations shown in Fig. 16(a). (b) Reconstructed velocity profiles that correspond to TR-PIV realizations shown in Fig. 16(c).

layer roll-up, and the flow goes to a fully separated state, as seen in Fig. 15 at $16\Delta t$. Interestingly, at this time instant, y_d crosses the point of inflection in the wall-normal direction [Fig. 17(a)], which leads to $y_d/y_{in} > 1$. This satisfies the absolute instability criterion proposed by Avanci *et al.* [62]. Moreover, the value of MRV(=29%) also satisfies the absolute instability criterion of the velocity profile proposed by Alam and Sandham [23]. From the $21\Delta t$ instant onward (i.e., when the larger vortices originate, as seen in Fig. 15), both the absolute instability criteria as mentioned above are satisfied [see Fig. 17(a) from 21 – $41\Delta t$ instants]. This observation indicates that absolute instability may be a source for the generation of coherent vortical structures in the separated shear layer.

However, while a separated flow changes from a completely separated state to an attached state, heights of the points of inflection decrease with time, as shown in Fig. 17(b). The point of inflection is also seen to cross over y_d in the wall-normal direction. This indicates that the velocity profiles go to an absolutely stable state. Furthermore, the MRV values for the velocity profiles also decrease with time, eventually leading to negate the absolute instability criterion of Alam and Sandham [23] (see Fig. 17(b) at $41\Delta t$ instant). The vortical structures are also found to be absent at this time instant.

Results presented in Sec. III E at $\alpha = 13^\circ$ show that the reduction in the low-frequency oscillation is mainly due to the continuous supply of backflow to the upstream from a vortical structure generated downstream. Hence, it is tempting to ask the question: Does the absolute instability criterion prevail for the longer time for $\alpha = 13^\circ$, as compared to the case of $\alpha = 11^\circ$? Therefore, similar to the case of $\alpha = 11^\circ$, the reconstructed velocity profiles for $\alpha = 13^\circ$ are also shown in Figs. 18(a) and 18(b). These figures show that the absolute instability criteria are satisfied based on both the MRV values and $y_d > y_{in}$ for all the velocity profiles; y_{in} does not cross over the y_d in

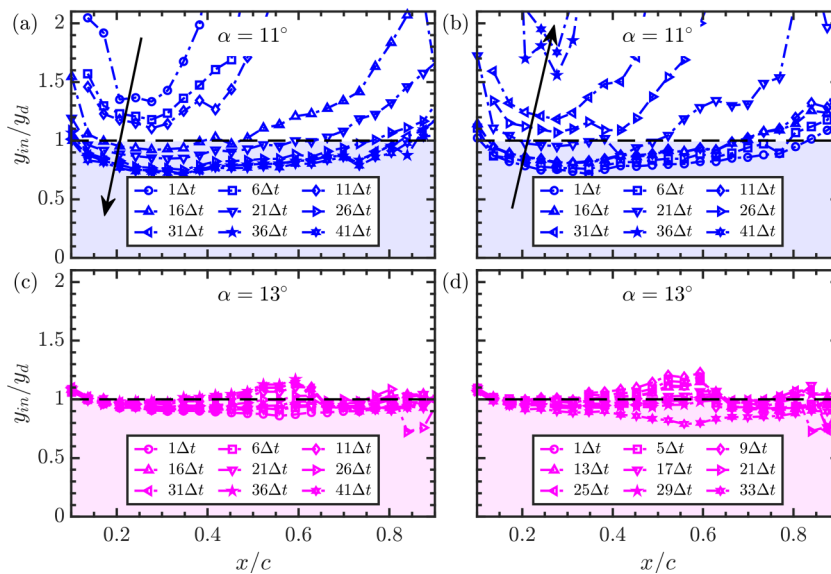


FIG. 19. Space-time variation of y_{in}/y_d calculated from the reconstructed velocity profiles using the first POD mode. (a) Corresponding to the TR-PIV realizations shown in Fig. 15(a). (b) Corresponding to the TR-PIV realizations shown in Fig. 15(c). (c) Corresponding to the TR-PIV realizations shown in Fig. 16(a). (d) Corresponding to the TR-PIV realizations shown in Fig. 16(c). The shaded region represents the absolutely unstable region according to the criterion of Avanci *et al.* [62]. The direction of the arrow indicates increasing time in panels (a) and (b).

any of the velocity profiles, in contrast to the case of $\alpha = 11^\circ$. This implies that these absolutely unstable velocity profiles at $\alpha = 13^\circ$ make the vortex-shedding process more regular and reduce the vertical oscillation of the shear layer.

Instead of investigating the absolute instability condition of Avanci *et al.* [62] at a particular streamwise location, several locations are considered to check the streamwise extension of the absolutely unstable region with time. The space-time variation of y_{in}/y_d is shown in Fig. 19. When the flow goes from attached to a completely separated state, the variation of y_{in}/y_d is shown in Fig. 19(a), which shows that the velocity profiles are absolutely stable not locally but also at all the spatial locations, at the time instant $1\Delta t$. However, the velocity profiles are absolutely unstable for all the spatial locations at the time instant $41\Delta t$. This indicates the possibility of changing the flow states from globally stable to unstable. Similar y_{in}/y_d variations are observed when the flow goes from a completely separated state to an attached state, as shown in Fig. 19(b). In contrast to the case of $\alpha = 11^\circ$, the velocity profiles are always found to be absolutely unstable at all x/c locations for $\alpha = 13^\circ$ case, except for $0.45 < x/c < 0.65$. A small increase in the value of y_{in}/y_d within $0.45 < x/c < 0.65$ is due to the secondary recirculation region with positive velocity values close to the wall. As a result, y_d value decreases, leading to an increase in y_{in}/y_d values. It is interesting to note the two-fold effect of the y_{in}/y_d on the flow state at $\alpha = 11^\circ$. When the flow goes from the attached to the separated state or from the separated to the attached state, the y_{in}/y_d values cross 1, as shown in Figs. 19(a) and 19(b), respectively. Therefore, while $y_{in}/y_d = 1$, the flow may go either to the attached or the separated state in the subsequent time instants, depending on the increase/decrease of y_{in}/y_d values. This increase/decrease of y_{in}/y_d values depends on the backflow received from the downstream vortical structure, which may in turn act as a controlling parameter.

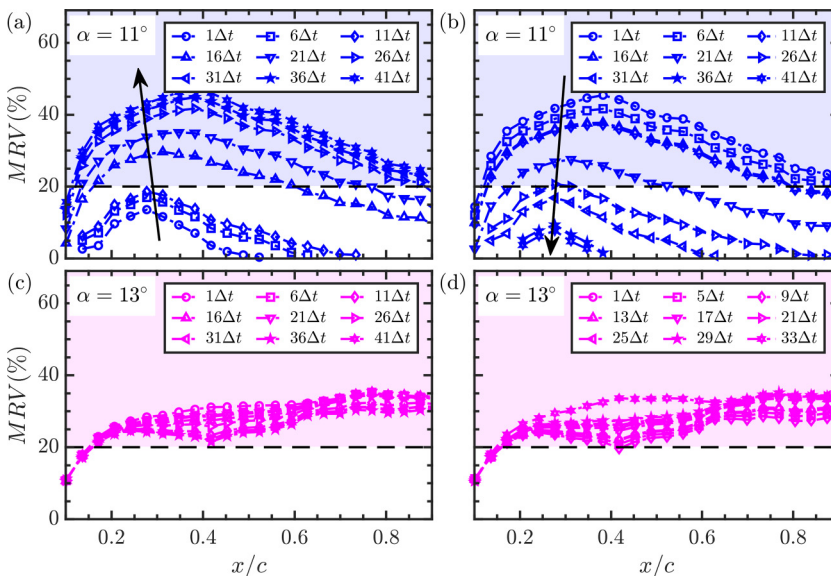


FIG. 20. Space-time variation of MRV calculated from the reconstructed velocity profiles using the first POD mode. (a) Corresponding to the TR-PIV realizations shown in Fig. 15(a). (b) Corresponding to the TR-PIV realizations shown in Fig. 15(c). (c) Corresponding to the TR-PIV realizations shown in Fig. 16(a). (d) Corresponding to the TR-PIV realizations shown in Fig. 16(c). The shaded region represents the absolutely unstable region according to the criterion of Alam and Sandham [23]. The direction of the arrow indicates increasing time in panels (a) and (b).

Furthermore, the space-time variation of MRV is also estimated to find the evolution of absolute instability region using the criteria of Alam and Sandham [23], as shown in Fig. 20. The MRV region is found to gradually extend in the streamwise direction with time, as shown in Fig. 20(a), corresponding to the time instants at which the flow goes from an attached state to a completely separated state. The MRV region extends in the streamwise direction, and the amount of backflow increases with time, leading to the global increase in the backflow region. Though it starts to increase from the time instant $1\Delta t$, it does not satisfy the absolute instability criterion of Avanci *et al.* [62] or Alam and Sandham [23] till the time instant $11\Delta t$. The increase in the backflow till $11\Delta t$ may be attributed to the small convective structures that may emerge due to the convective instability [for instance, see Fig. 15(b) for time instants 1– $11\Delta t$]; this is addressed in the next section. However, the flow satisfies the absolute instability criteria after the time instant $11\Delta t$. Eventually, the absolute instability criteria satisfy almost at all x/c locations, as was also found in the space-time variation of y_{in}/y_d [see Fig. 19(a)]. Similarly, when the flow goes from a completely separated state to an attached state [Fig. 15(d)], the MRV regions [Fig. 20(b)] are also found to be consistent with space-time variation of y_{in}/y_d , as shown in Fig. 19(b). For the case of $\alpha = 13^\circ$ the significant variation is not found in the MRV regions [Figs. 20(c) and 20(d)], as seen in the case of $\alpha = 11^\circ$. Moreover, it always satisfies the absolute instability criteria for $x/c > 0.15$, which indicates the possibility of global instability. Therefore, the results obtained from the two absolute instability criteria suggest that intermittent massive separation may be due to changing the flow state from globally stable to globally unstable.

The above absolute instability criteria are proposed based on the analytical velocity profiles by Avanci *et al.* [62] and the simulated velocity profiles over a flat plate geometry by Alam and Sandham [23], which may not be appropriate for the present study. Therefore, we have carried out a spatiotemporal stability analysis in the following section to confirm the above observations.

G. Spatiotemporal linear stability analysis

Linear stability analysis is often carried out to find the stability characteristics of a fluid dynamical system perturbed with a small infinitesimal disturbance (q). For such analysis, the disturbance is usually considered as the normal mode form. For two dimensional disturbance (q), it can be expressed as $\mathbf{q}(x, y, t) \sim \hat{\mathbf{q}}(y)e^{i(kx - \omega t)}$ where k and ω are wave number and frequency, respectively; here $\mathbf{q}(x, y, t) = [u, v, p]^T$, where u , v and p are the streamwise disturbance velocity, wall-normal disturbance velocity and the pressure disturbance, respectively. Using the normal mode form of the disturbances and the parallel flow approximation in the Navier–Stokes equation, one can obtain the following Orr-Sommerfeld equation (OSE) [see [63–65], for details],

$$(kU_b - \omega)[\hat{v}'' - k^2\hat{v}] - kU_b''\hat{v} = -\frac{i}{\text{Re}}[\hat{v}'''' - 2k^2\hat{v}'' + k^4\hat{v}], \quad (6)$$

where U_b is the base flow velocity, and the prime ($'$) indicates the derivative with respect to y ; here for normalization, the boundary layer edge velocity ($U_{e,r}$) and the displacement thickness (δ^*) are used as the velocity and length scales, respectively. These scales are also used to normalize the equation 6. Some previous studies demonstrated that the linear stability analysis can predict the vortex shedding characteristics even though the flow is not exactly parallel [e.g., Refs. [38,53,54,59]]. Diwan and Ramesh [66] justified the parallel flow approximation for the separation bubbles, using the condition $d(V/U)/dy = 0$, except at the turning point, i.e., at $U = 0$. Further, for the linear stability analysis, various types of base velocity profiles, such as steady velocity profile, mean velocity profile, short distance spatially averaged velocity profile, quasi-steady velocity profile, and unsteady/time-varying velocity profile, have been considered in the literature [e.g., Refs. [15,35,37,67–70]]. For example, Michelis *et al.* [15] and Hack and Zaki [70] carried out the spatial stability analysis for the velocity profile at different time instants to investigate the time variation of the stability characteristics. Following these works, we used the reconstructed and curve-fitted velocity profiles, similar to those shown in Figs. 17 and 18, for the stability analysis in the present study. It should be noted here that the velocity profiles were reconstructed using the first POD mode, which is a low-frequency mode, as discussed earlier. Such slowly time-varying velocity profiles can be used as base velocity profiles if the slow diffusion/low-frequency timescale (t_d) is larger than the convective/instability timescale (t_c) [15,69,71].

Following the work of Hall and Parker [71], ratio of the diffusion timescale to the convective timescale for the present work can be written as $\text{Re} = U_e\delta/\nu$, which is found to vary 10^3 – 10^4 for the velocity profiles considered in the present study. In addition, one can also estimate the ratio of the low-frequency and the convective timescales from the first (a_1) and the fourth (a_4) time-coefficients of the uv -POD modes at $\alpha = 11^\circ$, as these modes are associated with the low-frequency oscillation of the separated shear layer and the vortex shedding, respectively. From this estimate also, we found that the low-frequency timescale is reasonably higher ($\sim 10^1$) than the vortex shedding/instability timescale. This indicates that the quasi-steady approach [15,69,71] is applicable to the present study. Furthermore, the variation of $d(V/U)/dy$ in the wall-normal direction (not shown here for brevity) was also found to be nearly zero except at the turning point for both $\alpha = 11^\circ$ and $\alpha = 13^\circ$, as reported by Diwan and Ramesh [66]. Therefore, the parallel flow approximation is also applicable to the velocity profiles considered in the present study.

For the numerical solution of the above equation, a velocity profile is discretized using the spectral collocation method at the Gauss–Lobatto points $y_j = \cos(\frac{j\pi}{N_y})$ [64,65]. We used 180 points ($j = 0, 1, \dots, N_y - 1$) for discretizing a velocity profile in the y direction. For the given values of k (complex numbers), equation 6 is solved with the boundary conditions $\hat{v} = \hat{v}' = 0$ at the wall ($y = 0$) and the far-field ($y \rightarrow \infty$), which yields the local dispersion relation, $D(\omega, k) = 0$. The ω values in the complex k plane form the saddle point where $\partial\omega/\partial k = 0$ [62,65]. The values of ω and k at the saddle point are called the absolute frequency (ω_0) and the wave number (k_0). The real and imaginary parts of ω_0 are the angular frequency ($\omega_{0,r}$) and the temporal growth rate ($\omega_{0,i}$) of the disturbance wave. If $\omega_{0,i} > 0$, then the velocity profile is called absolutely unstable,

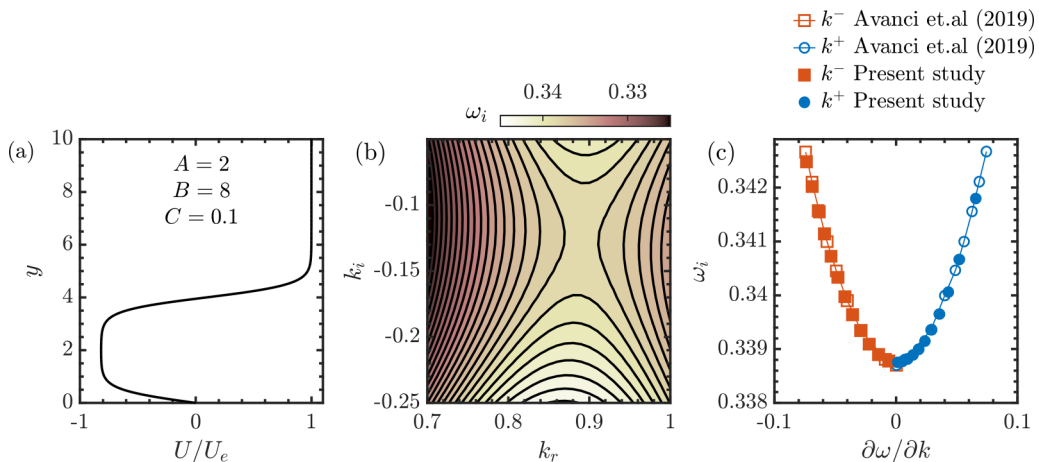


FIG. 21. Validation of the spatiotemporal stability analysis results. (a) Velocity profile corresponding to the profile P3 mentioned in Avanci *et al.* [62]. (b) Contours of temporal growth rate ω_i in the complex k plane. (c) Temporal growth rate ω_i versus group velocity $C_g = \partial\omega/\partial k$.

whereas it is called convectively unstable if $\omega_{0,i} < 0$ [22,24,72]. The present linear stability code has been validated with the results of Avanci *et al.* [62]. They used an analytical velocity profile, $U(y)/U_e = \{\tanh(Ay)[\tanh(Ay - B) + C]\}/(1 + C)$, for the spatiotemporal stability analysis, as shown in Fig. 21(a). We used this velocity profile with the given constants and solved equation (6) for validation purposes. Figures 21(b) and 21(c) show the ω_i contour in the complex k plane and the variation of ω_i against $\partial\omega/\partial k$, respectively. These spatiotemporal stability results show an excellent agreement with Avanci *et al.* [62].

As mentioned earlier, we used the curve-fitted velocity profiles at different x/c locations and at different instants of time to investigate the spatiotemporal stability characteristics. For example, Figs. 17 and 18 show the curve-fitted velocity profiles at $x/c = 0.3$ location but at different instants of time. Similarly, we used the curve-fitted velocity profiles at different x/c locations, as well, for the spatiotemporal stability characteristics.

Figure 22(a) shows the variations of both the temporal ($\omega_{0,i}$) and spatial ($k_{0,i}$) growth rates of the reconstructed velocity profiles corresponding to the TR-PIV realizations shown in Fig. 15(a). The left and right-hand sides of y axis correspond to $\omega_{0,i}$ and $k_{0,i}$, respectively. The symbols corresponding to $\omega_{0,i}$ and $k_{0,i}$ are also displayed with the same colors of their respective y axis. It should be noted that the saddle points were not observed at some streamwise locations where the separated region is found to be very small. Similar observations are also reported for a flow over an airfoil in the literature [e.g., Ref. [73]]. This may be attributed to the negligible amount of back flow near the reattachment region where the velocity profiles are comparatively fuller with high level of velocity fluctuations than those at initial stages of a separation bubble. However, this needs further attention. We plotted the $\omega_{0,i}$ and $k_{0,i}$ at those locations where the saddle point was clearly observed for the case of $\alpha = 11^\circ$ [for example, see time instants 1–11 Δt in Fig. 22(a)]. Due to the variation of δ_I^* and $U_{e,I}$ with time and space, $\omega_{0,i}$ and $k_{0,i}$ are normalized using U_∞ and chord length (c) for the better comparison. At time instant 1 Δt , the flow is in the attached state [see Fig. 15(b)]. The velocity profiles at this time instant (along x/c) show the flow is convectively unstable ($\omega_{0,i} < 0$). As time progresses, $\omega_{0,i}$ value increases, reaching the positive values almost at all the x/c locations at the time instant 16 Δt . Comparing Figs. 20(a) and 22(a), one observes that the increasing $\omega_{0,i}$ values are related to an increase of MRV values. Furthermore, at the initial time instants (1–11 Δt), the velocity profiles are convectively unstable, and the MRV values are also increasing at this time instants. This indicates that a convective instability may be the reason for the increase of the MRV values at

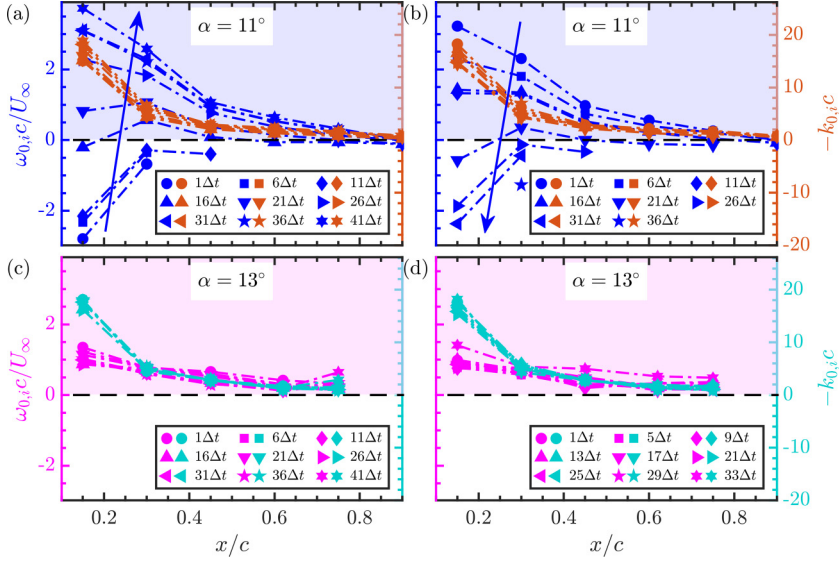


FIG. 22. Space-time variation of temporal growth rate estimated from the reconstructed velocity profiles using the first POD mode. (a) Corresponding to the TR-PIV realizations shown in Fig. 15(a). (b) Corresponding to the TR-PIV realizations shown in Fig. 15(c). (c) Corresponding to the TR-PIV realizations shown in Fig. 16(a). (d) Corresponding to the TR-PIV realizations shown in Fig. 16(c). The shaded region represents an absolutely unstable region according to the local stability analysis. The direction of the arrow indicates increasing time in panels (a) and (b), for $\omega_{i,0}$.

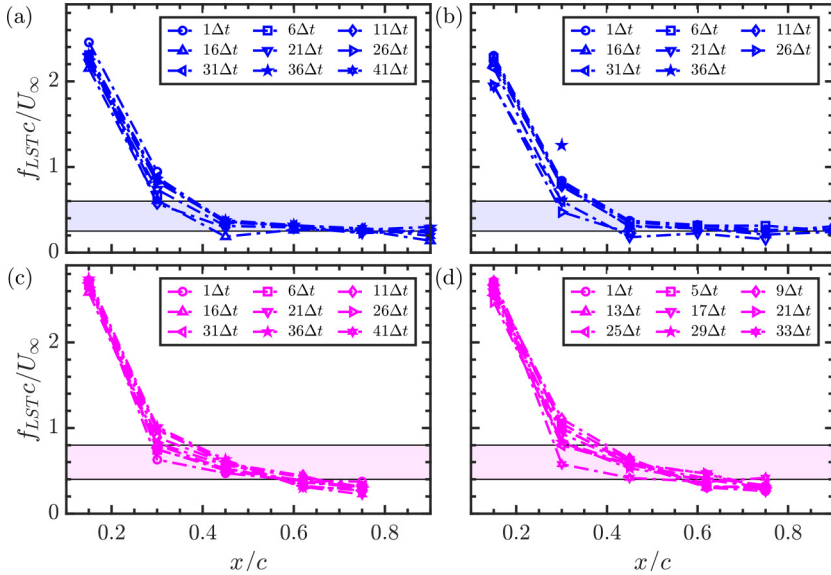


FIG. 23. Space-time variation of most amplified frequency estimated from the reconstructed velocity profiles using the first POD mode. (a) Corresponding to the TR-PIV realizations shown in Fig. 15(a). (b) Corresponding to the TR-PIV realizations shown in Fig. 15(c). (c) Corresponding to the TR-PIV realizations shown in Fig. 16(a). (d) Corresponding to the TR-PIV realizations shown in Fig. 16(c). The shaded region in panels (a), (b) and (c), (d) represents the experimentally measured peak-frequency band from the Figs. 9(b) and 9(d), respectively.

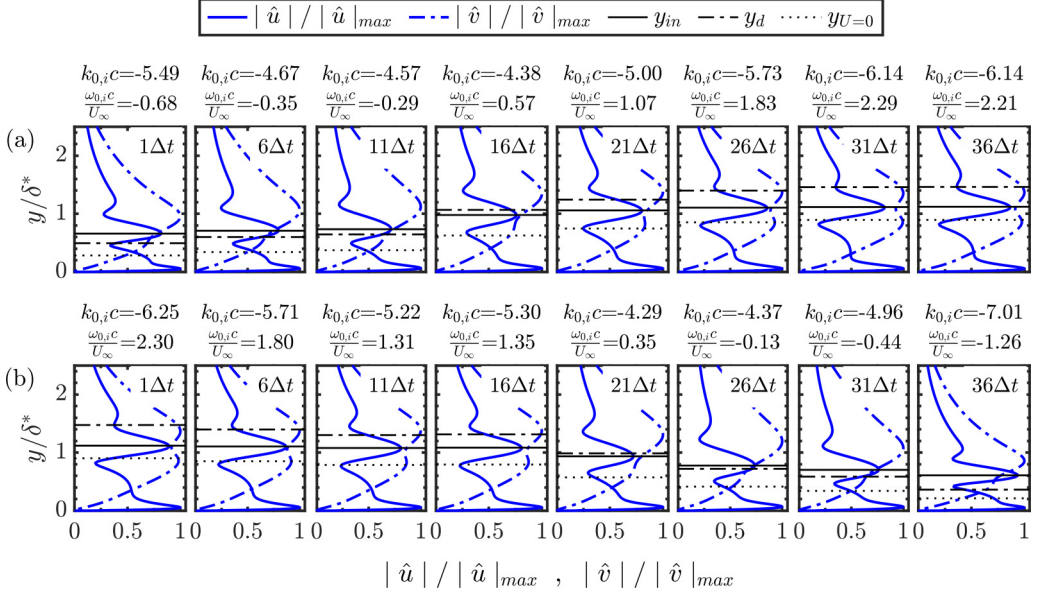


FIG. 24. The temporal variation of the eigenmodes for $\alpha = 11^\circ$, at $x/c = 0.3$. (a) Corresponding to the velocity profiles shown in Fig. 17(a). (b) Corresponding to the velocity profiles shown in Fig. 17(b).

the time-instants $1-11\Delta t$. The presence of convective instability is also confirmed by the spatial stability analysis of the velocity profiles at these time instants, but the results are not presented here for brevity. For the time instants greater than $16\Delta t$, the entire velocity profiles along x/c become absolutely unstable, which is consistent with the other absolute instability criteria discussed in the previous Sec. III F. Similarly, when the flow goes from a completely separated state to an attached state [Fig. 15(c)], $\omega_{0,i}$ values gradually decrease with time, and eventually go to negative values, as shown in Fig. 22(b). This implies a change of state from an absolutely unstable to convectively unstable state. For the case of $\alpha = 13^\circ$, the $\omega_{0,i}$ values, corresponding to Figs. 16(a) and 16(c), show the velocity profiles are always absolutely unstable, as shown in Fig. 22(c) and 22(d), respectively. This implies that the flow may be globally unstable at all time instants.

The most amplified frequency is calculated from the real part of the absolute frequency, i.e., $f_{LST} = \omega_{0,r}/2\pi$. Figure 23 shows the variation of $f_{LST} = \omega_{0,r}/2\pi$ for both cases of $\alpha = 11^\circ$ and 13° . The variation at a particular location is found to be insignificant at different time instants, whereas significant variation in the local f_{LST} can be noticed at different x/c locations. Moreover, the frequency decreases in the downstream locations. This may be attributed to the combined effect of y_{in} locations and the MRV values. Investigations of the analytical velocity profiles in some previous studies show that a higher MRV value in the velocity profile can lead to a lower frequency, and a higher y_{in} leads to an increase in the frequency [62,74]. In the intermittent separation process, the MRV and shear layer height change simultaneously. For example, when the flow goes from an attached state to a separated state, both MRV and δ^* values increase with time. The simultaneous increase in MRV and δ^* leads to a nearly constant frequency with time. This indicates that the prediction of f_{LST} is difficult solely based on the MRV or just based on the shear layer height. But interestingly, f_{LST} asymptotically becomes comparable with the experimental frequency band (shaded region in Fig. 23) toward the trailing edge region, indicating the possible location of the wavemaker [24,37] close to the trailing edge.

Figure 24 shows the time variation of the eigenmode shapes corresponding to the velocity profile in Fig. 17 at $x/c = 0.3$ for $\alpha = 11^\circ$. The eigenmodes, corresponding to the time instants at which the flow goes from an attached state to a completely separated state [Fig. 17(a)], and from a completely

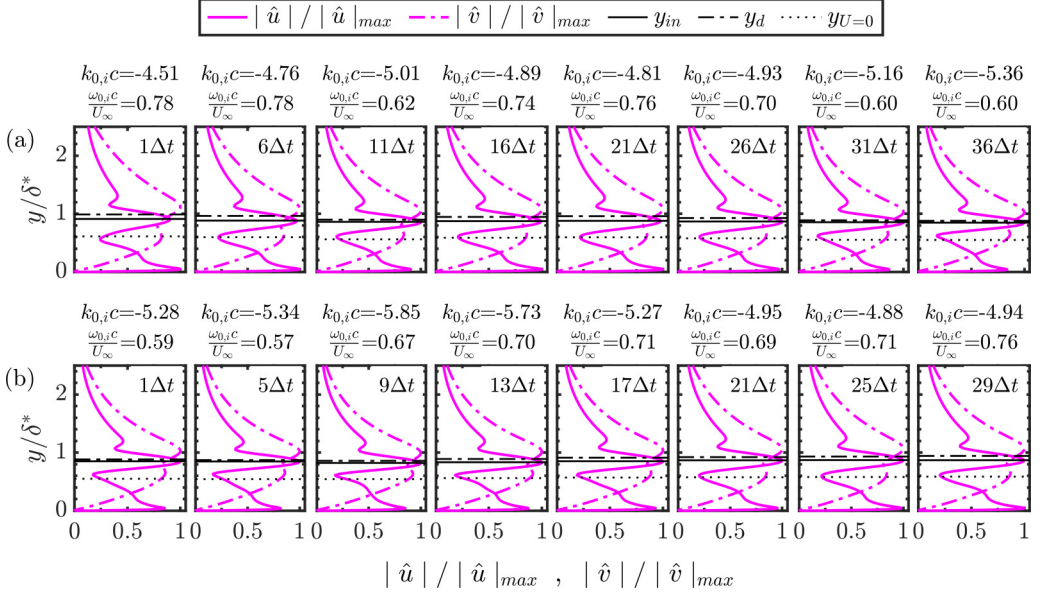


FIG. 25. The temporal variation of the Eigenmodes for $\alpha = 13^\circ$, at $x/c = 0.3$. (a) Corresponding to the velocity profiles shown in Fig. 18(a). (b) Corresponding to the velocity profiles shown in Fig. 18(b).

separated state to an attached state [Fig. 17(b)], are shown in Figs. 24(a) and 24(b), respectively. Moreover, the velocity profiles also show the change of the stability state (convective to absolute) at $x/c = 0.3$, as can be deduced from Fig. 22(a); hence we chose $x/c = 0.3$ to show the eigenmode variation at different time instants. It should be noted that y has been normalized by the displacement thickness estimated from the mean velocity profile at $x/c = 0.3$. The location of the y_{in} , y_d and height of the recirculating region ($y_{U=0}$) are superimposed with the eigenmode shapes for better comparison. In addition, the values of $k_{0,i}c$ and $\omega_{0,i}$ are also shown on top of each panel in Fig. 24. At time instant $1\Delta t$ in Fig. 24(a), the eigenmode associated with the streamwise velocity, \hat{u} , shows the two peaks: one is near the location of y_{in} , and another is inside the location of recirculating region. Even though one of the peaks of \hat{u} profile lies inside the recirculating region, it may not be associated with the upstream propagation of the disturbance as the instability is found to be convective in nature (i.e., $\omega_{0,i} < 0$) at this time instant. When the velocity profile becomes absolutely unstable (at time instant $16\Delta t$), both the peaks of \hat{u} profile, one inside the recirculating region and another at the inflection point, lie below the y_d . Similar features are also observed in the absolutely unstable eigenmodes of Avanci *et al.* [62]. Presence of absolute instability leads to an upstream propagation of a disturbance, which can be related to the supply of backflow to the upstream direction. This could be the reason for the abrupt growth of the separated region. For instance, one can see Fig. 15 at time instants 16–41 Δt . The same characteristics continue till the time instant 41 Δt , which makes the self-sustained oscillation. Similarly, both peaks of \hat{u} lie below the y_d for the time instants 1–21 Δt , as shown in Fig. 24(b). This corresponds to the time instants at which the flow is in a completely separated state [see Fig. 15(d)]. Moreover, the $\omega_{0,i}$ value is also positive, indicating the existence of an upstream propagation of the disturbance. At time instant 26 Δt , the $\omega_{0,i}$ value goes to a negative value, which is indicative of a convectively unstable state, and this can be related to the absence of backflow supply to the upstream direction. In both convectively and absolutely unstable states, the shapes of the eigenmodes are found to be similar. The only difference is the location of the \hat{u}_{peak} relative to y_d .

The eigenmode shapes corresponding to the velocity profiles in Figs. 18(a) and 18(b) are shown in Figs. 25(a) and 25(b), respectively. No significant variation can be noticed in the eigenmode

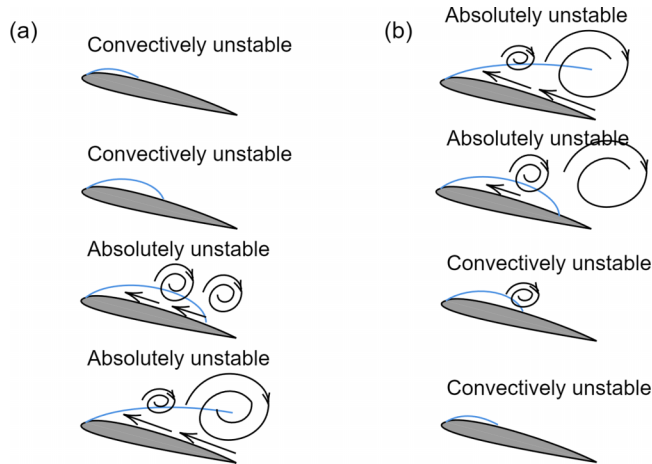


FIG. 26. A schematic to illustrate the mechanism of intermittent massive separation. (a) Attached to separated state, (b) separated to attached state. The temporal evolution of the separation bubble is shown by a blue colored line.

shapes. Even the location of \hat{u}_{peak} does not change significantly. This is expected as the velocity profiles are always absolutely unstable, for this case. This may lead to self-sustained oscillation, as the velocity profiles are found to be absolutely unstable at all time instants.

IV. CONCLUSIONS

The surface pressure measurements and the TR-PIV measurements are carried out to investigate the unsteady flow characteristics over an upper surface of NACA-0012 aerofoil at chord-based Reynolds number, $\text{Re}_c = 5 \times 10^4$. The instantaneous flow fields are investigated for the four angles of attack, i.e., at $\alpha = 10^\circ, 11^\circ, 12^\circ, 13^\circ$. The mean flow results show that the flow is separated over the entire surface of an aerofoil and satisfies the absolute instability criteria for the case of $11^\circ, 12^\circ, 13^\circ$. However, the complete separation is seen to be intermittent in the instantaneous TR-PIV realizations. This was identified by the instantaneous displacement thickness, δ_1^* . When δ_1^* reaches its minimum value in its variation, the flow in the major part of the upper surface was found to be in the attached state and vice versa.

The time sequence of the instantaneous flow field and the POD analysis are utilized to understand the mechanism of the intermittent massive separation, as summarized below. A small separated region is formed near the leading edge, and then it grows temporally without any significant vortex shedding. However, the height of the separated shear layer increases in the process of its temporal growth phase. Consequently, the shear layer becomes inflectionally unstable and sheds the vortices downstream. These shedding vortices convect downstream and supply the backflow in the upstream direction. As a result, the height of the separated shear layer increases in the upstream direction, leading to stronger and larger vortices. Finally, the flow goes to a completely separated state. While the larger vortex gets distorted and loses its coherent pattern, the strength of the vortex and the supply of the backflow in the upstream direction reduce, leading to a reduction in the shear layer height. In the process, the size of the separation bubble reduces, leading the flow over a major part of an upper surface to the attached state. A simple schematic is shown in Fig. 26 to explain the mechanism of this intermittent separation process.

A spatiotemporal stability analysis has also been carried out for the reconstructed local velocity profiles to understand their stability characteristics in this process. When a separated region is in the reattached state, the local stability analysis shows that the flow is convectively unstable. When the flow is in a completely separated state without reattachment, it is found to be absolutely unstable.

This indicates the upstream propagation of the disturbance, which is related to the supply of the backflow to the upstream direction from the downstream vortical structure, as shown schematically in Fig. 26(a). This is also found to be consistent with the streamline contour, as shown in Fig. 15(b). However, when the massive separated region goes to an attached state, the stability characteristics of the flow change from an absolutely unstable state to convectively unstable state [Fig. 26(b)]. The absolute instability characteristics are also found to be consistent with the absolute instability criteria proposed in the literature [23,62]. Thus these analyses clearly demonstrate that the intermittent massive separation process is related to the change of the stability characteristics of the velocity profiles from convectively unstable state to an absolutely unstable state and vice versa.

ACKNOWLEDGMENTS

The authors gratefully acknowledge the financial support received from the Indian Institute of Technology, Kanpur, for the TR-PIV system. We sincerely thank Prof. V. Shankar and Prof. K. Poddar for sharing their high-resolution CMOS camera and aerofoil, respectively. We also thank Prof. S. S. Gopalakrishnan for some fruitful discussions. We thank Mr. Siva Vignesh and the members of the low-speed aerodynamics laboratory for their assistance in performing the experiments. We sincerely thank all the referees of this article for their insightful comments and suggestions.

APPENDIX

The POD analysis of the fluctuating v velocity component is termed the v -POD analysis. We carried out this analysis for all the cases since it is suitable to characterize the shedding characteristics of the separated flow [see Refs. [27,75], for details]. A similar procedure, as was followed for the uv -POD analysis, is also used even for the v -POD analysis. Instead of using both the fluctuating velocity components, only the v component is used here. Figure 27 shows that the first two modes contribute a nearly equal amount of energy for all the cases. Further, this figure shows that the relative energy of the first two modes increases with increasing α . This is attributed to the high v fluctuation that occurs due to the highly organized coherent structures with increasing angle of attack.

The spatial mode shapes of the first two modes are found to be similar with a just spatial shift, as shown in Fig. 28. The time coefficients of the first two modes are also found to be similar with just a shift in time, as shown in Fig. 29. This space-time shift indicates that the first two modes are associated with a convective structure. The power spectra, estimated from the time coefficients, are shown in Figs. 29(e)–29(h). The spectra of the time coefficients corresponding to the first two

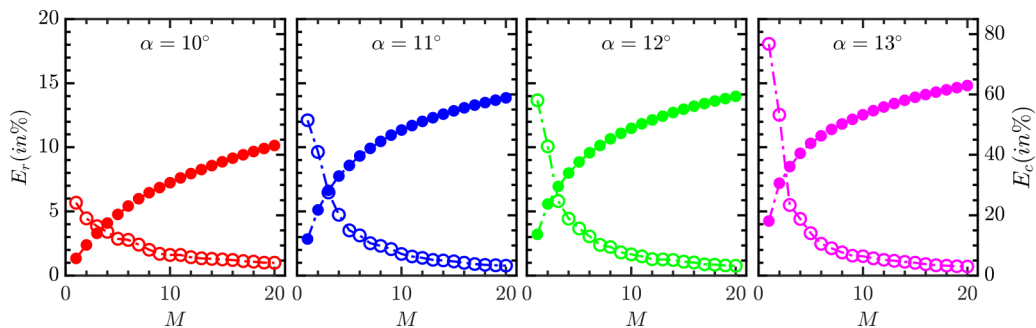


FIG. 27. Variation of the relative and cumulative energy levels of the v -POD modes for $\alpha = 10^\circ$, 11° , 12° , and 13° . Open symbols correspond to the relative energy (E_r) level and closed symbols correspond to the cumulative energy (E_c) level.

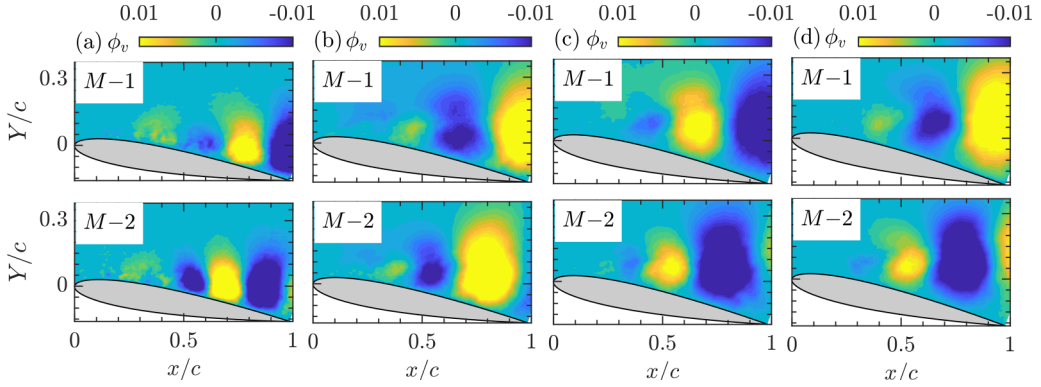


FIG. 28. First two energetic v -POD modes. (a) $\alpha = 10^\circ$, (b) $\alpha = 11^\circ$, (c) $\alpha = 12^\circ$, (d) $\alpha = 13^\circ$.

modes estimated from the v -POD analysis are found to be nearly similar. Moreover, these power spectra nearly match with the power spectra of the higher order modes of the uv POD modes. The power spectra of the uv -POD modes, $M-5$, $M-4$, $M-3$, $M-3$ for $\alpha = 10^\circ$, 11° , 12° , 13° , respectively, match with the power spectra of $M-1$ and $M-2$ of the v -POD modes. This may be attributed to the generation of the convective structure at those uv -POD modes. This also implies that the contribution of the convective structure to the total fluctuating field is enhanced with increasing α .

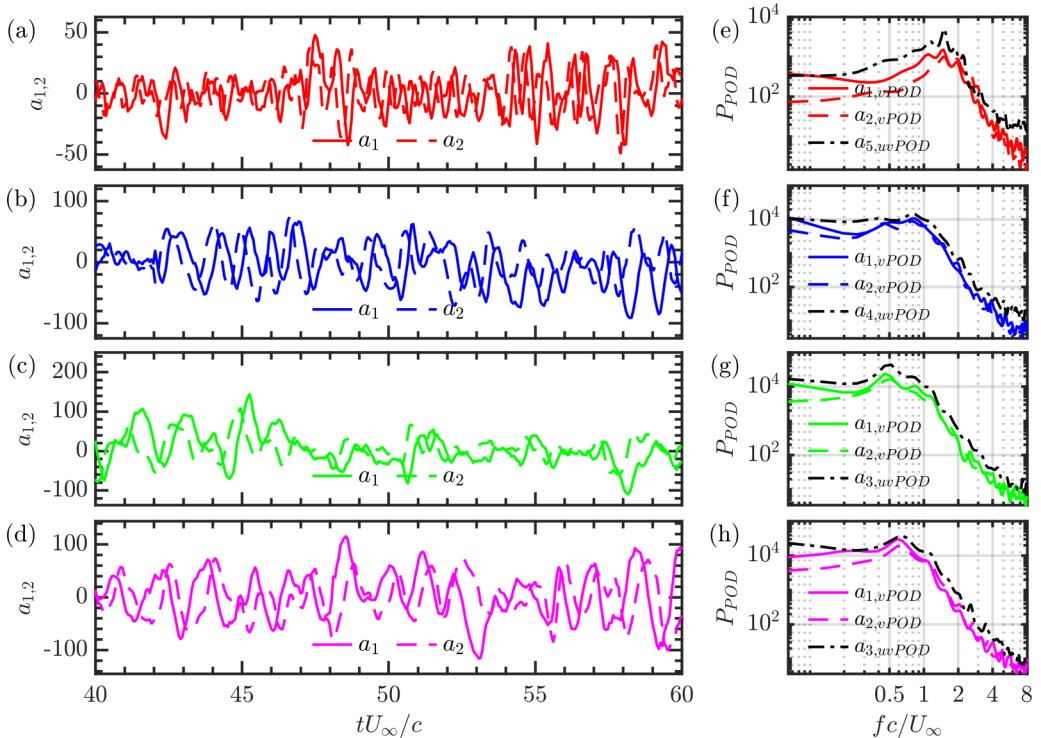


FIG. 29. Comparison of the time coefficients of the first two v -POD modes and their power spectra. v -POD time coefficients, (a) $\alpha = 10^\circ$, (b) $\alpha = 11^\circ$, (c) $\alpha = 12^\circ$, (d) $\alpha = 13^\circ$; v -POD frequency spectra, (e) $\alpha = 10^\circ$, (f) $\alpha = 11^\circ$, (g) $\alpha = 12^\circ$, (h) $\alpha = 13^\circ$.

- [1] J. Winslow, H. Otsuka, B. Govindarajan, and I. Chopra, Basic understanding of airfoil characteristics at low Reynolds numbers (10 4–10 5), *J. Aircr.* **55**, 1050 (2018).
- [2] E. Eljack, J. Soria, Y. Elawad, and T. Ohtake, Simulation and characterization of the laminar separation bubble over a NACA-0012 airfoil as a function of angle of attack, *Phys. Rev. Fluids* **6**, 034701 (2021).
- [3] H. P. Horton, Laminar separation bubbles in two and three dimensional incompressible flow, PhD. thesis, Queen Mary University of London, 1968.
- [4] P. R. Owen and L. Klanfer, On the laminar boundary layer separation from the leading edge of a thin aerofoil, Technical report (Aeronautical Research Council, London, UK, 1953).
- [5] I. Tani, Low-speed flows involving bubble separations, *Prog. Aerosp. Sci.* **5**, 70 (1964).
- [6] M. Gaster, *The Structure and Behavior of Laminar Separation Bubbles*, Technical Report 3595, Aeronautical Research Council, 1967.
- [7] S. S. Diwan, S. J. Chetan, and O. N. Ramesh, On the bursting criterion for laminar separation bubbles, In *Proceedings of the IUTAM Symposium on Laminar-Turbulent Transition* (Springer, Berlin, 2006), pp. 401–407.
- [8] M. Kiya and K. Sasaki, Structure of a turbulent separation bubble, *J. Fluid Mech.* **137**, 83 (1983).
- [9] N. J. Cherry, R. Hillier, and M. E. M. P. Latour, Unsteady measurements in a separated and reattaching flow, *J. Fluid Mech.* **144**, 13 (1984).
- [10] A. Mohammed-Taifour and J. Weiss, Unsteadiness in a large turbulent separation bubble, *J. Fluid Mech.* **799**, 383 (2016).
- [11] J. AlMutairi, E. ElJack, and I. AlQadi, Dynamics of laminar separation bubble over NACA-0012 airfoil near stall conditions, *Aerospace Sci. Technol.* **68**, 193 (2017).
- [12] A. V. Dovgal, V. V. Kozlov, and A. Michalke, Laminar boundary layer separation: Instability and associated phenomena, *Prog. Aerosp. Sci.* **30**, 61 (1994).
- [13] J. H. Watmuff, Evolution of a wave packet into vortex loops in a laminar separation bubble, *J. Fluid Mech.* **397**, 119 (1999).
- [14] S. S. Diwan and O. N. Ramesh, On the origin of the inflectional instability of a laminar separation bubble, *J. Fluid Mech.* **629**, 263 (2009).
- [15] T. Michelis, S. Yarusevych, and M. Kotsonis, Response of a laminar separation bubble to impulsive forcing, *J. Fluid Mech.* **820**, 633 (2017).
- [16] M. Kiya and K. Sasaki, Structure of large-scale vortices and unsteady reverse flow in the reattaching zone of a turbulent separation bubble, *J. Fluid Mech.* **154**, 463 (1985).
- [17] P. R. Spalart and M. Kh. Strelets, Mechanisms of transition and heat transfer in a separation bubble, *J. Fluid Mech.* **403**, 329 (2000).
- [18] R. Hain, C. J. Kähler, and R. Radespiel, Dynamics of laminar separation bubbles at low-Reynolds-number aerofoils, *J. Fluid Mech.* **630**, 129 (2009).
- [19] J. H. Almutairi and I. M. AlQadi, Large-eddy simulation of natural low-frequency oscillations of separating–reattaching flow near stall conditions, *AIAA J.* **51**, 981 (2013).
- [20] K. B. M. Q. Zaman, D. J. McKinzie, and C. L. Rumsey, A natural low-frequency oscillation of the flow over an airfoil near stalling conditions, *J. Fluid Mech.* **202**, 403 (1989).
- [21] J. H. Almutairi, L. E. Jones, and N. D. Sandham, Intermittent bursting of a laminar separation bubble on an airfoil, *AIAA J.* **48**, 414 (2010).
- [22] D. A. Hammond and L. G. Redekopp, Local and global instability properties of separation bubbles, *Eur. J. Mech. B. Fluids-B/Fluids* **17**, 145 (1998).
- [23] M. Alam and N. D. Sandham, Direct numerical simulation of “short” laminar separation bubbles with turbulent reattachment, *J. Fluid Mech.* **410**, 1 (2000).
- [24] D. Rodríguez, E. M. Gennaro, and L. F. Souza, Self-excited primary and secondary instability of laminar separation bubbles, *J. Fluid Mech.* **906**, A13 (2021).
- [25] N. Alferez, I. Mary, and E. Lamballais, Study of stall development around an airfoil by means of high fidelity large eddy simulation, *Flow Turbul. Combust.* **91**, 623 (2013).
- [26] O. Marxen and D. S. Henningson, The effect of small-amplitude convective disturbances on the size and bursting of a laminar separation bubble, *J. Fluid Mech.* **671**, 1 (2011).

- [27] S. Mohamed Aniffa and A. Ch. Mandal, Experiments on the low-frequency oscillation of a separated shear layer, *Phys. Rev. Fluids* **8**, 023902 (2023).
- [28] M. Embacher and H. F. Fasel, Direct numerical simulations of laminar separation bubbles: investigation of absolute instability and active flow control of transition to turbulence, *J. Fluid Mech.* **747**, 141 (2014).
- [29] C. Jagadeesh and H. Fasel, Experimental investigation of the structure and dynamics of laminar separation bubbles, In *Proceedings of the 50th AIAA Aerospace Sciences Meeting Including the New Horizons Forum and Aerospace Exposition* (AIAA, 2013), p. 755.
- [30] S. Siva Viknesh and K. Poddar, Active control of separated flow on a symmetric airfoil by pitching oscillation, *Phys. Fluids* **33**, 087115 (2021).
- [31] D. M. Sharma and K. Poddar, Investigations on quasi-steady characteristics for an airfoil oscillating at low reduced frequencies, *Int. J. Aerosp. Eng.* **2010**, 940528 (2010).
- [32] E. M. Eljack and J. Soria, Investigation of the low-frequency oscillations in the flowfield about an airfoil, *AIAA J.* **58**, 4271 (2020).
- [33] T. Ohtake, Y. Nakae, and T. Motohashi, Nonlinearity of the aerodynamic characteristics of NACA0012 aerofoil at low Reynolds numbers, *Japan Soc. Aeronaut. Space Sci.* **55**, 439 (2007).
- [34] K. Rinoie and N. Takemura, Oscillating behaviour of laminar separation bubble formed on an aerofoil near stall, *Aeronaut. J.* **108**, 153 (2004).
- [35] G. Balamurugan and A. C. Mandal, Experiments on localized secondary instability in bypass boundary layer transition, *J. Fluid Mech.* **817**, 217 (2017).
- [36] S. M. Aniffa and A. C. Mandal, Experimental investigation on the role of the streaky-like structures in a pressure-induced separation bubble, In *Proceedings of 16th Asian Congress of Fluid Mechanics* (Springer, Berlin, 2021), pp. 267–276.
- [37] D. Dutta, I. Kanshana, S. S. Gopalakrishnan, and A. C. Mandal, Experimental studies on the frequency selection in flat plate wakes: Mean-flow stability analyses and low-dimensional modeling, *Phys. Rev. Fluids* **7**, 044102 (2022).
- [38] S. M. Aniffa, V. S. Caesar, V. Dabaria, and A. C. Mandal, Characteristics of geometry-and pressure-induced laminar separation bubbles at an enhanced level of free-stream turbulence, *J. Fluid Mech.* **957**, A19 (2023).
- [39] A. C. Mandal and J. Dey, An experimental study of boundary layer transition induced by a cylinder wake, *J. Fluid Mech.* **684**, 60 (2011).
- [40] H. W. Coleman and W. G. Steele, *Experimentation, Validation, and Uncertainty Analysis for Engineers* (John Wiley & Sons, New York, NY, 2018).
- [41] J. P. Holman, *Experimental Methods for Engineers* (McGraw Hill, New York, NY, 2012).
- [42] M. Raffel, C. E. Willert, F. Scarano, C. J. Kähler, S. T. Wereley, and J. Kompenhans, *Particle Image Velocimetry: A Practical Guide* (Springer, Berlin, 2018).
- [43] W. Thielicke, The flapping flight of birds: Analysis and application, Ph.D. thesis, University of Groningen, 2014.
- [44] E. L. Houghton and P. W. Carpenter, *Aerodynamics for Engineering Students* (Elsevier, Amsterdam, 2003).
- [45] M. V. Lowson, S. P. Fiddes, and E. C. Nash, Laminar boundary layer aeroacoustic instabilities, in *Proceedings of the 32nd AIAA Aerospace Sciences Meeting and Exhibit, AIAA-Paper 94-0358* (AIAA Press, Reston, VA, 1994), pp. 1–10.
- [46] E. Arcondoulis, C. Doolan, and A. C. Zander, Airfoil noise measurements at various angles of attack and low Reynolds number, In *Proceedings of ACOUSTICS* (Australian Acoustical Society, 2009), pp. 23–25.
- [47] S. Pröbsting, F. Scarano, and S. C. Morris, Regimes of tonal noise on an airfoil at moderate Reynolds number, *J. Fluid Mech.* **780**, 407 (2015).
- [48] V. Golubev, Recent advances in acoustics of transitional airfoils with feedback-loop interactions: A review, *Appl. Sci.* **11**, 1057 (2021).
- [49] M. S. Istvan and S. Yarusevych, Effects of free-stream turbulence intensity on transition in a laminar separation bubble formed over an airfoil, *Exp. Fluids* **59**, 52 (2018).
- [50] J. W. Kurelek, M. Kotsonis, and S. Yarusevych, Transition in a separation bubble under tonal and broadband acoustic excitation, *J. Fluid Mech.* **853**, 1 (2018).

- [51] Z. Yang and I. E. Abdalla, Effects of free-stream turbulence on large-scale coherent structures of separated boundary layer transition, *Int. J. Numer. Methods Fluids* **49**, 331 (2005).
- [52] Z. Yang and I. E. Abdalla, Effects of free-stream turbulence on a transitional separated–reattached flow over a flat plate with a sharp leading edge, *Int. J. Heat Fluid Flow* **30**, 1026 (2009).
- [53] W. Balzer and H. F. Fasel, Numerical investigation of the role of free-stream turbulence in boundary-layer separation, *J. Fluid Mech.* **801**, 289 (2016).
- [54] M. S. H. Boutilier and S. Yarusevych, Separated shear layer transition over an airfoil at a low Reynolds number, *Phys. Fluids* **24**, 084105 (2012).
- [55] I. Rodríguez, O. Lehmkuhl, R. Borrell, and A. Oliva, Direct numerical simulation of a NACA0012 in full stall, *Int. J. Heat Fluid Flow* **43**, 194 (2013).
- [56] L. Sirovich, Turbulence and the dynamics of coherent structures. I. Coherent structures, *Q. Appl. Math.* **45**, 561 (1987).
- [57] A. C. Mandal, L. Venkatakrishnan, and J. Dey, A study on boundary-layer transition induced by free-stream turbulence, *J. Fluid Mech.* **660**, 114 (2010).
- [58] D. Lengani, D. Simoni, M. Ubaldi, and P. Zunino, Pod analysis of the unsteady behavior of a laminar separation bubble, *Exp. Therm Fluid Sci.* **58**, 70 (2014).
- [59] S. Hosseinverdi and H. F. Fasel, Numerical investigation of laminar–turbulent transition in laminar separation bubbles: The effect of free-stream turbulence, *J. Fluid Mech.* **858**, 714 (2019).
- [60] O. Marxen and U. Rist, Mean flow deformation in a laminar separation bubble: Separation and stability characteristics, *J. Fluid Mech.* **660**, 37 (2010).
- [61] M. Nishioka, M. Asai, and S. Yoshida, Control of flow separation by acoustic excitation, *AIAA J.* **28**, 1909 (1990).
- [62] M. P. Avanci, D. Rodríguez, and L. S. de B. Alves, A geometrical criterion for absolute instability in separated boundary layers, *Phys. Fluids* **31**, 014103 (2019).
- [63] F. M. White and J. Majdalani, *Viscous Fluid Flow*, Vol. 3 (McGraw-Hill, New York, NY, 2006).
- [64] Dan S, P. J. Schmid, and D. S. Henningson, Transition to turbulence, in *Stability and Transition in Shear Flows* (Springer, Berlin, 2001), pp. 401–475.
- [65] M. P. Juniper, A. Hanifi, and V. Theofilis, Modal stability theory: Lecture notes from the FLOW-NORDITA summer school on advanced instability methods for complex flows, Stockholm, Sweden, 2013, *Appl. Mech. Rev.* **66**, 024804 (2014).
- [66] S. S. Diwan and O. N. Ramesh, Relevance of local parallel theory to the linear stability of laminar separation bubbles, *J. Fluid Mech.* **698**, 468 (2012).
- [67] S. S. Gopalakrishnan and A. C. Mandal, Transient growth in a flat plate boundary layer under a stream with uniform shear, *Phys. Fluids* **33**, 114101 (2021).
- [68] J. Philip, M. Karp, and J. Cohen, Streak instability and generation of hairpin-vortices by a slotted jet in channel crossflow: Experiments and linear stability analysis, *Phys. Fluids* **28**, 014103 (2016).
- [69] A. Nayak and D. Das, Transient growth of optimal perturbation in a decaying channel flow, *Phys. Fluids* **29**, 064104 (2017).
- [70] M. J. P. Hack and T. A. Zaki, Streak instabilities in boundary layers beneath free-stream turbulence, *J. Fluid Mech.* **741**, 280 (2014).
- [71] P. Hall and K. H. Parker, The stability of the decaying flow in a suddenly blocked channel, *J. Fluid Mech.* **75**, 305 (1976).
- [72] P. Huerre and P. A. Monkewitz, Local and global instabilities in spatially developing flows, *Annu. Rev. Fluid Mech.* **22**, 473 (1990).
- [73] L. E. Jones, R. D. Sandberg, and N. D. Sandham, Direct numerical simulations of forced and unforced separation bubbles on an airfoil at incidence, *J. Fluid Mech.* **602**, 175 (2008).
- [74] U. Rist and U. Maucher, Investigations of time-growing instabilities in laminar separation bubbles, *Eur. J. Mech. B. Fluids-B/Fluids* **21**, 495 (2002).
- [75] D. Simoni, D. Lengani, M. Ubaldi, P. Zunino, and M. Dellacasagrande, Inspection of the dynamic properties of laminar separation bubbles: Free-stream turbulence intensity effects for different Reynolds numbers, *Exp. Fluids* **58**, 66 (2017).